HHS Public Access

Author manuscript

Dev Biol. Author manuscript; available in PMC 2017 July 15.

Published in final edited form as:

Dev Biol. 2016 July 15; 415(2): 278–295. doi:10.1016/j.ydbio.2015.12.024.

MEMO1 drives cranial endochondral ossification and palatogenesis

Eric Van Otterloo[1], **Weiguo Feng**[1], **Kenneth L Jones**[2], **Nancy E Hynes**[3,4], **David E Clouthier**[1], **Lee Niswander**[5,6], and **Trevor Williams**[1,5,6]

[1] Department of Craniofacial Biology, University of Colorado Anschutz Medical Campus, Aurora, CO, 80045, USA [2] Department of Biochemistry and Molecular Genetics, University of Colorado School of Medicine, Aurora, Colorado 80045 USA [3] Friedrich Miescher Institute for Biomedical Research, Maulbeerstrasse 66, CH-4058 Basel, Switzerland [4] University of Basel, CH-4002 Basel, Switzerland [5] Department of Cell and Developmental Biology, University of Colorado Anschutz Medical Campus, Aurora, CO, 80045, USA [6] Department of Pediatrics, University of Colorado Anschutz Medical Campus, Children's Hospital Colorado, Aurora, CO 80045, USA

Abstract

The cranial base is a component of the neurocranium and has a central role in the structural integration of the face, brain and vertebral column. Consequently, alteration in the shape of the human cranial base has been intimately linked with primate evolution and defective development is associated with numerous human facial abnormalities. Here we describe a novel recessive mutant mouse strain that presented with a domed head and fully penetrant cleft secondary palate coupled with defects in the formation of the underlying cranial base. Mapping and non-complementation studies revealed a specific mutation in *Memo1* - a gene originally associated with cell migration. Expression analysis of *Memo1* identified robust expression in the perichondrium and periosteum of the developing cranial base, but only modest expression in the palatal shelves. Fittingly, although the palatal shelves failed to elevate in *Memo1* mutants, expression changes were modest within the shelves themselves. In contrast, the cranial base, which forms via endochondral ossification had major reductions in the expression of genes responsible for bone formation, notably matrix metalloproteinases and markers of the osteoblast lineage, mirrored by an increase in markers of cartilage and extracellular matrix development. Concomitant with these changes, mutant cranial bases showed an increased zone of hypertrophic chondrocytes accompanied by a reduction in both vascular invasion and mineralization. Finally, neural crest cell-specific deletion of *Memo1* caused a failure of anterior cranial base ossification indicating a cell autonomous role for MEMO1 in the development of these neural crest cell derived structures. However, palate formation was largely normal in these conditional mutants, suggesting a non-autonomous role for MEMO1 in palatal closure. Overall, these findings assign a new function to MEMO1 in driving endochondral ossification in the cranium, and also link

abnormal development of the cranial base with more widespread effects on craniofacial shape relevant to human craniofacial dysmorphology.

Keywords

Endochondral ossification; cranial base; cleft palate; palatogenesis; neural crest; MEMO1

Introduction

The human head skeleton is composed of two integrated components, the viscerocranium (also termed the splanchnocranium) and the neurocranium. The viscerocranium makes up the face and associated structures, while the neurocranium includes the cranial vault along with the underlying cranial base. The cranial base serves as a central integration point for development, growth, evolution and function of the craniofacial complex [1-3]. Specifically, the cranial base provides a structural platform from which the cranial vault and viscerocranium grow. In addition, it houses the pituitary and sense organs of the head, links the cranium with the trunk via its connection with the vertebral column, and provides a structure through which the cranial vessels and nerves traverse [2]. Thus, abnormalities in the size or flexion of the cranial base can impact overall facial shape and are often an underlying component of several human craniofacial defects [4-6]. Moreover, changes in the morphology of the cranial base are a critical aspect of the alterations in primate facial shape and brain growth that occurred during human evolution [1,2]. Despite the importance of the cranial base, there are only a limited number of animal model systems that provide information concerning its unique developmental program.

In mammals, the cranial base is derived from two major embryonic cell populations, the neural crest (anterior cranial base) and mesoderm of cranial paraxial and somitic origin (posterior cranial base) [7-9]. This is in contrast to the cartilage and bone of the viscerocranium, which is largely neural crest cell derived [10,11]. In addition, the cranial base develops through endochondral ossification, whereas the viscerocranium forms largely through intramembranous ossification [12]. The cranial base initially develops from a series of cartilages that fuse to form the mature chondrocranium by about E16.5 of mouse development [7,13]. Subsequently, a number of ossification centers arise in the midline resulting in a rostral-caudal progression of the presphenoid, basisphenoid and basioccipital bones of the cranial base by birth. Each pair of bones is separated by a cartilaginous synchondrosis that is important to allow continued growth of the cranial base until maturity [4,7]. Therefore, the transition between cartilage and bone in the cranial base must be tightly regulated with both temporal and spatial resolution to allow normal growth and function. Generation of ossified bone during endochondral ossification is a well-documented process in which mesenchymal precursors first form a cartilage intermediate before being replaced by bone [14,15]. As such, this process involves defined stages of cartilage maturation, vascular invasion, and subsequent mineralization by bone forming osteoblasts [14,15]. In contrast, intramembranous ossification involves the conversion of mesenchymal precursors into bone forming osteoblasts directly, without a cartilage intermediate [14,15]. Given these distinct developmental processes, unique gene-regulatory programs and biological

mechanisms likely drive ossification of these two bone groupings in the head. Supporting this, differences in vascular invasion have been observed between endochondral and intramembranous bones of the human fetal head, and animal models exist with defects in a distinct subset of these craniofacial bones [16,17]. However, given the final product of both mechanisms is ossified bone, there are also likely overlapping genetic programs involved, although the degree of dependency on these programs may be different between these two bone populations [12]. Teasing out these dependencies may provide insight into the etiologies of various osteogenic disorders affecting subsets of bones in the craniofacial complex.

To identify genes and alleles affecting mouse craniofacial formation we have recently conducted a recessive N-ethyl-N-nitrosourea (ENU) screen [18]. Here we report the phenotypic and molecular characterization of one mutant from this screen that displayed a combination of craniofacial defects including cleft secondary palate, a domed cranium, and cranial base defects. We identified the affected gene responsible for these defects as *Memo1 (Mediator of Erbb2 Driven Cell Motility 1),* which encodes a multi-functional protein originally linked with cell migration and metastasis in breast cancer [19-21]. Mice homozygous for a *Memo1* null mutation have previously been shown to die beginning at E13.5, accompanied by severe vasculature defects [22]. However, no craniofacial defects were noted in these null embryos. Therefore, our analysis indicates a novel role for MEMO1 in craniofacial development, and further suggests that some instances of human cleft palate may arise secondary to defects in development of the cranial base.

Results

Identification and characterization of the F1-9-13FP mutant

Following ENU treatment of C57BL/6J male mice, we generated founder males that were used in a three-generation cross to screen for recessive mutations that lead to defects in head morphology at embryonic day 18.5 (E18.5) [18]. From this, we identified a mutant line that we originally termed F1-9-13FP in which ~25% of the offspring from heterozygous matings displayed a variety of craniofacial defects including a misshapen nasal bridge, a downward positioned cranium, a domed skull (Fig 1A, C), and a fully penetrant cleft palate (Fig 1B, D). When these mice were allowed to develop to term, they did not thrive, and displayed no milk in their stomachs, consistent with the cleft palate defect (Table 1).

To probe the underlying skeletal organization in F1-9-13FP homozygous mutants, we processed embryos for bone and cartilage analysis. The bones of the head are mainly derived from either of two embryonic populations, the neural crest or mesoderm [7,11,13,23]. In addition, the majority of the craniofacial bones are formed through intramembranous ossification, although a subset are formed through endochondral ossification [12,13]. Initial examination of E18.5 craniofacial skeletons revealed that the most severely affected bones were those of neural crest cell origin, especially those that undergo endochondral ossification (Fig 1E-J). The endochondral bones of the cranial base - the presphenoid, basisphenoid, and the basioccipital - were of particular interest in this regard as fate mapping studies have shown that these bones and their cartilage templates are derived from neural crest cells, neural crest cells and cranial paraxial mesoderm, or somitic mesoderm, respectively [7-9]. Notably, in F1-9-13FP homozygous mutants, the degree of hypoplasia of

these bones correlated with the extent of their neural crest cell origin, with the presphenoid often absent (a small remnant remains in some instances), the basisphenoid very hypoplastic, and the basioccipital only slightly affected compared with controls (Fig 1G,H). In addition to the cranial base, other endochondral bones including the neural crest cell derived hyoid [11,13] and the mesoderm derived otic capsule [24], also failed to ossify in F1-9-13FP homozygous mutants (Fig 1G,H).

Although endochondral bones were the most severely affected, a subset of neural crest cell derived intramembranous elements of the viscerocranium, including the premaxillary, maxillary, and palatine bones were also hypoplastic in F1-9-13FP homozygous mutants as compared to controls (Fig 1E, F). Several additional craniofacial skeletal elements also showed defects, including the palatal processes of the palatine and maxillary bones, which were absent (Fig 1 E, F), and the bones of the calvaria, which were more widely separated and appeared less ossified overall in F1-9-13FP homozygous mutants than in controls (Fig 1I, J). In common with the cranial base, the majority of the bones of the trunk and appendicular skeleton are derived via endochondral ossification. The majority of these bones had a normal appearance in homozygous F1-9-13FP mutants, although we did note reduced ossification of several bones at the extremities, specifically the phalanges and the xiphoid process of the sternum (data not shown). Therefore, there does not appear to be a generalized defect in endochondral ossification in the mutants. Instead, our analysis indicates that the mutation present in the F1-9-13FP strain has the greatest impact on the neural crest cell derived endochondral bones of the head, and to a lesser extent, additional neural crest cell and mesoderm derived intramembranous craniofacial bones.

A point mutation in *Memo1 (Mediator of Erbb2 driven cell motility 1*) correlates with the F1-9-13FP phenotype

The ENU-mutagenized C57BL/6J founder male was outcrossed onto a wild type 129S1/SvImJ background for mapping and maintenance purposes. Meiotic recombination mapping enabled the approximate position of the mutation to be identified using polymorphic markers that distinguished between these two mouse strains. Initially, using markers spanning ~10 mega base pair (Mb) intervals throughout the mouse autosomes, the mutation was mapped to an ~45Mb region on chromosome 17 (between polymorphic markers D17Mit67 and D17Mit123) (Fig 2A). Subsequently, markers D17Mit40, D17Mit206, D17Mit142, and D17Mit76 were used to refine the position of the mutation to one of two possible 5-10Mb intervals. Next, genomic DNA from a mutant embryo was subjected to whole exome enrichment and sequencing. Inspection of the relevant intervals indicated that this mutant, as well as all subsequent mutants but not their littermate controls, were homozygous for a point mutation in an intron of *Mediator of ErbB2 induced cell motility 1*, or *Memo1* (Fig 2B). This point mutation maps to the interval between the previously identified markers D17Mit206 and D17Mit142, consistent with *Memo1* being the causative gene.

More specifically, the ENU-induced mutation was a single base-pair change in the splice donor of exon 8 of *Memo1*, converting the 5th nucleotide 3’ of the exon 8-intron 8 boundary from a guanine to an adenine (Fig 2B). Note that this mutation also creates a novel XmnI restriction site that can be used for genotyping confirmation (Fig 2B,C). Importantly,

previous studies have identified this 5th position 3' of an exon-intron boundary to be highly conserved and critical for proper mRNA splicing [25]. To assess the potential consequence of this point mutation on mRNA splicing, RNA was harvested from F1-9-13FP mutants and control embryos, cDNA synthesized, and PCR carried out using primers flanking exon 8 of *Memo1*. Depending on the primer pair used for analysis, a variety of aberrant splice products were detected in the mutants and no wild-type product was produced (data not shown). Cloning and sequencing of these splice products indicated a variety of mis-splicing events, although the most prominent appeared to be an exclusion of exon 8, resulting in an in-frame fusion of exon 7 and 9 (Fig 2D and Supplemental Fig 1). These observations were consistent with *Memo1* being the affected locus in F1-9-13FP mutants.

Genetic non-complementation and protein analysis indicates that F1-9-13FP mutants are MEMO1-null

Previously, *Memo1 null* mutants were observed to die beginning at ~E13.5, accompanied by vascular abnormalities, but defects in craniofacial development were not reported [22]. The differences in phenotype between *Memo1 null* and F1-9-13FP mutants suggest that if *Memo1* is responsible for the F1-9-13FP phenotype either the phenotype is dependent on genetic background and/or the ENU-induced mutation generates a hypomorphic allele. To distinguish between these possibilities, we outcrossed the ENU allele, which was generated on a C57BL/6J background, onto the 129S1/SvImJ background (>95% 129S1/SvImJ), the strain used for the previous *Memo1* mutant studies [22]. During successive out-crossings, no F1-9-13FP$^{(129S1/SvlmJ)}$ homozygous mutants were identified at late embryonic stages (E18.5). However, *Memo1* mutants were detected at earlier time-points (~E11.5-E14.5) and similar to earlier studies, these embryos displayed reduced vascular development within the yolk-sac (Fig 3A,B). In addition, in F1-9-13FP$^{(129S1/SvlmJ)}$ mutants, the embryo proper began to show defects in vasculogenesis, displaying a combination of unorganized blood vessel formation, general hemorrhaging and edema, associated with embryonic lethality evident around E12.5-E14.5 (Fig 3C,D and not shown).

In a reciprocal experiment, we used available targeted ES-cells from the European Conditional Mouse Mutagenesis (EUCOMM) repository to generate mice with a *Memo1^{ki}* allele (EUCOMM *tm1b* allele, referred to as *Memo1^{ki}* from this point forward) lacking exon 4, but containing a *LacZ* expression cassette (Supplemental Fig 2C) [26]. We subsequently generated *Memo1$^{ki/ki}$* offspring on a largely C57BL/6J background (>80%) and then assessed their embryonic phenotype. Examination of *Memo1$^{ki/ki}$* embryos at E18.5 identified a similar defect to that observed for F1-9-13FP mutants on the C57BL/6J background, namely a domed head, snout defects (Fig 3E, G) and clefting of the secondary palate (Fig 3F, H). Moreover, *Memo1$^{ki/ki}$* mutants were unable to thrive after birth, as none were found at weanling stages (P21-P28). In addition, genetic non-complementation analysis was carried out between the *Memo1^{ki}* allele and the F1-9-13FP allele on a largely C57BL/6J background and the resulting offspring assessed at E18.5. As anticipated, embryos harboring both the KI and ENU alleles displayed the aforementioned craniofacial defects, whereas heterozygous embryos were indistinguishable from control embryos (Fig 3I,J and not shown). Together, these findings support the hypothesis that the embryonic phenotypes associated with loss of MEMO1 are highly dependent on genetic background.

The similarity between the *Memo1*$^{ki/ki}$ and F1-9-13FP mutant phenotypes further suggested that the ENU-induced mutation generated a null allele. We therefore assayed MEMO1 protein expression using a monoclonal antibody that recognizes the N-terminus of MEMO1 [21]. Western blot analysis of protein isolated from E13.5 heads of either the F1-9-13FP mutants (Fig 3K) or *Memo1*$^{ki/ki}$ mutants (Supplemental Fig 3) showed a complete absence of protein in both instances indicating that the ENU induced mutation likely generates a null allele. In sum, genetic complementation coupled with protein analysis confirms: 1. *Memo1* is the affected locus in F1-9-13FP mutants (allele referred to as *Memo1*^{tm1Will} from this point forward); 2. genetic background alters the embryonic phenotype due to loss of MEMO1; and 3. the ENU-induced mutation generates a null allele.

Analysis of *Memo1* expression during embryonic craniofacial development

Expression analysis was next performed to gain insight into MEMO1's role during normal craniofacial development. Previous reports have identified a generally ubiquitous expression pattern for *Memo1* during embryonic development as well as expression within most adult organs [22,27]. However, a more thorough analysis of *Memo1* expression, specifically within the craniofacial region during key stages of development, has not been carried out. Therefore, using a combination of RNA *in situ* hybridization, the *Memo1*^{neo} *LacZ* reporter line (EUCOMM *tm1a* allele, referred to as *Memo1*^{neo} from this point forward, Supplemental Fig 2A), and global gene expression analysis, we more closely examined *Memo1* expression specifically within the developing head, focusing most heavily on the secondary palate and cranial base, given the defects observed in these structures (Fig 1). RNA expression profiling of the facial prominences indicated that *Memo1* was expressed in all three facial prominences, in both the ectoderm and mesenchyme, between E10.5-E12.5 (Supplemental Fig 4). Next, we employed whole mount analysis of *Memo1* RNA expression to refine the spatial expression pattern (Fig 4 A-C). At E10.5 *Memo1* RNA was detected throughout the facial prominences (frontonasal, maxillary, and mandibular) as well as in the 2nd branchial arch (Fig 4A, B). Interestingly, expression levels were not uniform, with highest signal seen at distal versus proximal locations in the facial prominences (Fig 4A, B). Elevated levels of *Memo1* expression were also detected in the distal limb buds at E10.5, and to a lesser extent in a segmented pattern in the developing trunk (Fig 4A). At E12.5 *Memo1* expression produced a more diffuse expression pattern in the developing facial prominences, with some enrichment in the developing lens and vibrissae (Fig 4C). For the analysis of later time-points, we utilized embryos heterozygous for the *Memo1*^{neo} *LacZ* knock-in allele (Supplemental Fig 2A) to study specific regions of the developing head. With respect to the secondary palate, analysis of E13.5 *Memo1*$^{neo/+}$ heads demonstrated β-galactosidase activity (i.e. *LacZ* expression) diffusely throughout the nasal side of the developing palatal shelf mesenchyme (Fig 4D). By E15.5, after the palatal shelves had fused, *LacZ* expression was reduced at the midline of the palate, but was enriched at the periphery near the developing maxillary bones, as well as locations internal to locations within these developing bones (Fig 4E, F). Expression was also detected in the presumptive perichondrium surrounding the nasal cartilage (Fig 4E). In contrast, expression in the ectoderm of the palatal shelves or nasal septum was far less prominent. Analysis of the cranial base at E15.5 revealed strong *LacZ* expression in the perichondrium and periosteum of the developing cartilage and bone, respectively (Fig 4G-J). Expression was also detected at lower levels in cells at various

stages of chondrocyte differentiation (resting, proliferative, hypertrophic) (Fig 4I) as well as internal to locations within these developing cranial base bones (Fig 4I, J). Other notable sites of enriched *LacZ* expression in the head included the tongue (Fig 4G), pituitary gland (Fig 4G, I), vibrissae (Fig 4K), and the choroid plexus (Fig 4G). In summary, although the expression of *Memo1* is extensive in the developing embryo, sites of enriched expression are evident within the facial prominences at E10.5. Furthermore, at later embryonic time-points *Memo1* expression occurs in the mesenchyme of the palatal shelves and associated with bones and cartilage of the cranial base, maxilla, and nasal septum consistent with the occurrence of defects in many of these structures.

Analysis of neural crest cell migration and palatogenesis in *Memo1^{m1Will}* mutants

Gross phenotype assessment and skeletal analysis indicated major defects in the secondary palate and cranial base in *Memo1^{m1Will}* mutants (Fig 1). To understand the mechanistic basis of these defects we conducted a variety of histological, molecular, and genetic studies on these two structures during development.

One common link between the secondary palate and the cranial base is that both have major contributions from neural crest cells. Moreover, MEMO1 has been previously linked with cell migration, a process that is also critical for neural crest cell contribution to the developing head [19,20,28]. Therefore, we began by studying general neural crest cell development and migration in *Memo1^{m1Will}* homozygous mutant mice. *Tfap2a* [29,30], *Inka1* [31], and *Hoxa2* [32] expression were used as markers of cranial neural crest cell migration and we determined that this process was equivalent between mutant and control embryos at E9.5 and E10.5 (Supplemental Fig 5A-D and not shown). Next, we employed anti-neurofilament immunostaining and *Sox10* RNA expression to study the differentiation of neural crest cells into peripheral nervous system components, including the cranial ganglia. Again, we did not detect any differences between mutant and control embryos in this assay (Supplemental Fig 5F, G and not shown). To assess later stages of neural crest cell migration into the developing palatal shelves, we utilized the combination of a Wnt1-Cre transgene and a rosa-Tomato reporter line [33,34]. Examination of labeled neural crest cells in the E13.5 palatal shelves of either control or *Memo1*-null embryos indicated successful population of the facial mesenchyme in both strains (Supplemental Fig 5H, I). Overall, these findings suggest that loss of MEMO1 does not cause a generalized defect in neural crest cell induction, migration or differentiation that would account for the observed craniofacial phenotypes.

Next, we performed a histological analysis of palatogenesis in *Memo1^{m1Will}* mutants and littermate controls to determine the step at which fusion failed. Serial frontal sections were H&E stained from E13.5 to E15.5, the time at which the palatal shelves normally elevate and fuse (Fig 5). At E13.5 in a wild-type embryo, the paired palatal shelves are growing parallel to the developing tongue (Fig 5A). Subsequently, by E14.5, the palatal shelves transition to a horizontal plane above the tongue and shortly thereafter the paired shelves meet at the midline and begin to fuse (Fig 5B). Finally, by E15.5 the epithelium at the midline of the fused palatal shelves (midline epithelial seam) is removed, resulting in a single contiguous layer of mesenchyme between the now fused shelves (Fig 5C). *Memo1^{m1Will}* mutants were initially indistinguishable at E13.5 from controls, but by E14.5

the palatal shelves had failed to elevate into the horizontal plane in both anterior and posterior positions of the developing palate (Fig 5D,E and data not shown). By E15.5, the palatal shelves remained separate as unfused remnants resulting in the presence of a cleft palate (Fig 5F). Since neural crest cells were able to populate the shelves (Supplemental Fig 5H, I), we next considered that their failed elevation might result from altered neural crest cell differentiation or cell proliferation. However, changes in gene expression (measured using RNA-Seq analysis or the examination of specific marker expression *in vivo*) or cell proliferation (measured using EdU incorporation) were relatively modest (Fig 5G-I and Supplemental Fig 5E, J-Q). In addition, late stage analysis of EdU incorporation (E14.5) or cell death (TUNEL, E15.5) in the palate did not identify major changes between control and *Memo1*^{m1Will} mutants (data not shown). Taken together, these results suggest that the failure of secondary palate closure in *Memo1*-null embryos either results from subtle defects within the shelves themselves or that it is secondary to developmental events occurring elsewhere in the *Memo1*-null mutant head.

Memo1^{m1Will} mutants show normal chondrocranium development but reduction in regulators of endochondral ossification in the cranial base

Next, to assess development of the cartilage anlage of the cranial base we stained control and *Memo1*^{m1Will} mutant embryos with alcian blue (Fig 6A-H). At E14.5, cartilage deposition in the anterior cranial base is slightly delayed in *Memo1*^{m1Will} mutants as compared to controls (Fig 6A,E). However, by E15.5, cartilage condensation and formation appears equivalent in the cranial base by gross examination in controls as compared to in *Memo1*^{m1Will} mutants (Fig 6B,F). By E16.5, alcian blue negative regions are evident in the mid and posterior cranial base of a control embryo, corresponding to zones of ossification in the basisphenoid and basioccipital, respectively, as seen by alizarin red staining (bone stain) at a similar stage (Fig 6C,D). By contrast, in *Memo1*^{m1Will} mutants at an identical developmental stage, the majority of the cranial base remained strongly stained with alcian blue (Fig 6G). This persistent staining corresponds with reduced ossification of the cranial base bones at a similar stage (Fig 6H). Overall, this analysis identified that development of the chondrocranium (cartilage condensation) proceeded largely unabated in *Memo1*^{m1Will} mutants. However, following condensation, replacement of cartilage with ossified bone failed to occur at control levels.

To assess the molecular changes associated with the difference in cranial base ossification we dissected cranial base tissue from both control and *Memo1*^{m1Will} mutants at E15.5 (3/group, similar to outlined region in Fig 6B and F) and analyzed global gene expression differences by RNA-seq. In contrast to the small number of statistically significant differences observed for the palatal shelves, gene expression differences for the cranial base were far more pronounced. Thus, *Memo1*^{m1Will} mutants showed ~300 genes significantly down-regulated and ~220 genes significantly upregulated (at $p<0.05$), as compared to controls (Fig 6I, Supplemental Table 1). Functional annotation of all genes showing significantly altered expression using DAVID [35] indicated that the most significantly affected categories encompassed the extracellular matrix, skeletal system development and mitochondrial function (Supplemental Table 1).

The degree of gene expression change was more pronounced in the down-regulated category, with ~20 genes showing a greater than 4-fold reduction in mapped transcripts in the mutant cranial base, while no genes were increased by more than 4-fold. Functional annotation clustering using genes most highly down-regulated ($p < 0.05$ and >1.35 fold-change, 139/520 significant genes) captured skeletal system and ossification categories (Supplemental Table 1). Prominent within the down-regulated category were genes involved in degradation of a collagen-based extracellular matrix (ECM) that are required for endochondral ossification, particular *Mmp13* and *Mmp9,* which were decreased by >30 fold and ~5 fold respectively (Fig 6J, upper panel) [36-39]. Several other genes involved with formation or modification of the extracellular matrix (*Acp5/TRAP*, *Spp1*, *Dmp1*, and *Ibsp*), as well as markers of the osteoblast lineage (*Sp7/Osterix*, *Col1a2*, and *Osr2*) were also expressed at significantly lower levels in the mutants, relative to controls (Fig 6J, upper panel) [40-46]. Conversely, functional annotation clustering of the most significantly upregulated genes ($p < 0.05$ and >1.35 fold-change, 123/520 significant genes) captured categories associated with cartilage development, cartilage condensation, and ECM (Fig 6J, lower panel, Supplemental Table 1). These genes included those encoding proteins involved in cell signaling (*Ihh*, *Fgfr3*, *Fgfrl1*), transcription factors (*Sox9*), and cartilage ECM proteins (*Acan/Aggrecan*, *Col2a1*, *Col9a1*, *Lect1*) [47-54]. In summary, global gene-expression profiling identified a significant reduction in expression of genes important for endochondral ossification, concomitant with an increase in expression of cartilage specific genes. These findings support those seen by the cartilage and bone staining (Fig 6), namely an inhibition of endochondral ossification at a stage subsequent to cartilage formation in *Memo1^{m1Will}* mutants. In addition, the data indicate these changes are associated with alterations in the expression of genes involved in formation and degradation of the ECM, as well as respiration, suggesting a complex interplay of several physiological processes in driving MEMO1-dependent cranial base development.

Reduced endochondral ossification in *Memo1^{m1Will}* mutants is associated with disrupted hypertrophic chondrocyte replacement, vascular invasion, and mineralization of the developing bone

Chondrocranium analysis by histology and RNA expression profiling indicated a failure of *Memo1^{m1Will}* mutants to transition from a cartilage template anlage to ossified bone (Fig 6). This transition has been well defined and includes precisely staged events marked by distinct cellular identities, including resting, proliferative, and hypertrophic chondrocytes, followed by vascular recruitment and subsequent invasion by proliferating osteoblasts, which promote bone mineralization [14,15]. Therefore, we examined the differentiation status of the cartilage and its associated vasculature in greater detail in *Memo1^{m1Will}* mutants versus controls using both histology and molecular marker analysis. To begin, we examined H&E midsagittal sections (Fig. 7A, B) through the cranial base at E15.5 and E18.5 in control and *Memo1^{m1Will}* mutants (Fig 7C-H). In particular, we focused on the basisphenoid bone, as this element is clearly affected in *Memo1^{m1Will}* mutants and its stages of ossification are well defined at these developmental stages. At E15.5, resting, proliferative, and hypertrophic cartilage zones were clearly demarcated in the cranial base of a control embryo (Fig 7C). Similar zones were evident at E18.5, although the hypertrophic chondrocyte zone was quickly replaced by mineralized bone matrix, forming the basisphenoid bone (Fig 7E, F). In

contrast, at E15.5 in *Memo1*^{m1Will} mutants, resting and proliferative zones were present, although the progression of hypertrophic chondrocytes was slightly perturbed, evident by these chondrocyte cells appearing less hypertrophic (enlarged) as compared to controls (Fig 7D). By E18.5, defects in cartilage to bone progression in the *Memo1*^{m1Will} mutant cranial base became even more evident. Although *Memo1*^{m1Will} mutants displayed grossly normal resting and proliferative zones, an abnormally elongated zone of hypertrophic chondrocytes was evident (Fig 7G, H). Concomitant with this exaggerated hypertrophic zone was a major reduction in matrix deposition within the region that would normally form the basisphenoid bone (Fig 7G, H). These findings suggest defects in cranial base ossification in *Memo1*^{m1Will} mutants are associated with a general failure in conversion of hypertrophic chondrocytes to mineralized bone.

A key event in promoting the transition from hypertrophic chondrocytes to ossified bone is the ECM remodeling activity of MMP9 and MMP13, which have been shown to free ECM bound VEGFA within the hypertrophic chondrocyte zone, allowing diffusion of the ligand to the perichondrium/periosteum, thus promoting vascular invasion and bone ossification [55,56]. Interestingly, expression profiling identified significant reductions in both *Mmp9* and *Mmp13* mRNA levels in the cranial base of *Memo1*^{m1Will} mutants (Fig 6J).

Previous studies in long bones have shown that perturbation of MMP9/MMP13 activity can result in a similar elongated zone of hypertrophic chondrocytes associated with reduced vascular invasion of this zone [38]. To assess the status of vascular recruitment into the hypertrophic zone of *Memo1*^{m1Will} mutants versus controls, we examined mid-sagittal sections of E15.5 and E18.5 embryos via anti-CD31 immunoreactivity, which marks endothelial cells of the developing vasculature [57]. In E15.5 control embryos, CD31+ cells surrounded the hypertrophic zone, in the perichondrium near the future basisphenoid bone (Fig 7I, arrowheads). By E18.5, this immunoreactivity was more prominent in the perichondrium and was seen throughout the mineralized portion of the basisphenoid bone (Fig 7J, K). By contrast, in *Memo1*^{m1Will} mutants, reduced CD31+ cells were seen lining the hypertrophic zone at E15.5 (Fig 7L). This reduction in CD31+ cells in the perichondrium of the hypertrophic zone was still evident at E18.5 and coincided with a failure of vascular invasion of the elongated hypertrophic zone of cartilage that occurs in place of the normal basisphenoid bone matrix (Fig 7M, N). Coincident with reduced vascular invasion, there was also a drastic reduction in the amount of EdU+, proliferating cells (presumed osteoblasts) within the developing basisphenoid bone of *Memo1*^{m1Will} mutants as compared to controls (Fig 7O, P). The observation that the vascular network does not surround the cartilage from E15.5 through E18.5 at levels similar to control embryos in the cranial base of the mutants, while general maturation of the embryo still occurs normally, also argues against the phenotype being caused by a generalized developmental delay. Instead, these results indicate that the loss of MEMO1 has a specific effect on the cranial base, with reduced mineralization of cranial base bones in *Memo1*^{m1Will} mutants associated with a failure of hypertrophic chondrocyte removal and a loss of vascular invasion of these skeletal elements.

MEMO1 acts cell-autonomously within the cranial neural crest cells during cranial base ossification but not for closure of the secondary palate

The secondary palate is derived from both neural crest cells and ectoderm, while the cranial base is composed of both neural crest cells and mesoderm derivatives. Therefore, we next sought to determine whether MEMO1 functions autonomously in the shared cranial neural crest cell component to drive both cranial base and palate development. The *Memo1*^{neo} allele was used as a starting point for generation of a conditional *Memo1* allele (EUCOMM *tm1c* allele, termed *Memo1*^{flp} from this point forward, Supplemental Fig 2B, see methods). Subsequently, mice homozygous for the *Memo1*^{flp} allele (*Memo1*$^{flp/flp}$) were bred with mice carrying the *Memo1*^{ki} allele plus the *Wnt1CRE* transgene, allowing precise deletion of MEMO1 from the developing neural crest cells (Supplemental Fig 2D) [33].

At E18.5, the gross external appearance of the *Memo1* conditional knockout (*Memo1*$^{NC-CKO}$) was similar to a milder version of the *Memo1*^{m1Will} mutant phenotype, with a slightly dipped nasal bridge, and a domed skull (Fig 8A, C). However, with the exception of one mutant, the majority of these embryos did not have a cleft palate (9 of 10; Fig 8B, D, E). Similar to *Memo1*^{m1Will} mutants, *Memo1*$^{NC-CKO}$ pups did not survive after birth, likely due to an inability to suckle as no milk was observed in the stomachs of mutants irrespective of the presence of an obvious cleft palate (data not shown). We next assessed the underlying skeleton of the mutants at E18.5 to determine the effect of the neural crest cell specific loss of MEMO1 on both the palate and the cranial base. For the majority of mice that did not have an overt cleft secondary palate we still noted hypoplastic development of both the palatal process of the palatine bone, and to a lesser extent the palatal process of the maxillary bone (Fig 8F,G). In contrast, the palatal bones in the single *Memo1*$^{NC-CKO}$ mutant that displayed a cleft palate more closely resembled those found in the *Memo1*^{m1Will} mutant (Compare Fig 8H and 1F). With respect to the cranial base, the presphenoid is the only bone that is derived from the neural crest [7], and in common with the *Memo1*^{m1Will} mutants this bone failed to ossify or was severely hypoplastic in the *Memo1*$^{NC-CKO}$ mutants (Fig 8I-K). In contrast, the basisphenoid was far less affected, displaying a mild rostral truncation, and the basioccipital had a normal appearance (Fig 8I-K). These latter two bones are derived from mesodermal cells (cranial paraxial and somitic, respectively) and their appearance was consistent with the lack of a direct neural crest cell influence on their phenotype. Examination of other bones in the cranial base and remaining craniofacial complex also largely supported a cell autonomous role for MEMO1 in the neural crest cells during skeletal development. Thus, the premaxilla was hypoplastic, and the hyoid failed to ossify in common with the *Memo1*^{m1Will} mutants (Fig 8I,J). In contrast, mesodermally derived bones, including the two small bones formed from the hypochiasmatic cartilages that flank the presphenoid bone, and the otic capsules, were less affected. These bones were absent in the *Memo1*^{m1Will} embryos but were visible in *Memo1*$^{NC-CKO}$ embryos (compare Fig 1H and Fig 8I-K). In addition, note that the single mutant that had a clear cleft secondary palate also had a more severely affected presphenoid (Fig 8K). Finally, regions corresponding to the neural crest cell derived metopic and coronal sutures were more widely spaced in *Memo1*$^{NC-CKO}$ as compared to controls (Supplemental Fig 6A, B). Taken together, these findings support a cell autonomous role for MEMO1 in the neural crest cells with respect to cranial base ossification, but also indicate that loss of MEMO1 in the mesenchyme of the

palatal shelves may not be the underlying cause of overt cleft secondary palate in *Memo1*-null embryos.

Discussion

Here we identify *Memo1*, a gene that encodes a previously described receptor tyrosine kinase (RTK)-adapter molecule and reactive oxygen species (ROS) generating redox enzyme, as a novel effector in promoting bone ossification, most notably in the cranial base [21,22]. The importance of MEMO1 in craniofacial development was initially identified through our recessive ENU-based forward genetic screen. Subsequently, non-complementation and protein analyses indicated that the ENU-induced mutation in *Memo1* results in a null allele. Moreover, our studies show that the embryonic phenotypes are strongly dependent on mouse genetic background. In agreement with previous studies, on a 129 background, the loss of MEMO1 results in mid-gestation lethality [22]. However, on a C57BL/6J background, *Memo1*-null mice can live to birth and display many craniofacial defects, particularly cleft secondary palate and alterations in the cranial base, a structure known to form through endochondral ossification. The cranial base has a major role in determining the morphology of the mammalian head, and the following features were consistently observed with respect to this central skeletal structure in *Memo1* mutants. First, the cranial base anlage, the chondrocranium, formed appropriately in the absence of *Memo1*, although there was a slight initial delay in its development. Second, as chondrocranium development progressed, replacement by ossified bone was defective, resulting in a persistent cartilage template. This observation was supported molecularly by RNA expression profiling of the cranial base, which identified an increase in transcripts associated with cartilage biology and a concomitant decrease in ossification associated transcripts in *Memo1* mutants. Third, reduced ossification coincided histologically with a loss of vascular invasion of the developing cranial base skeletal elements. Initially, this was seen as reduced vascular cells in the perichondrial lining of the cartilage hypertrophic zone and subsequently a loss of vascular invasion of the ossified bone itself. Fourth, the failure of bone mineralization was associated with an elongated zone of hypertrophic chondrocytes. Collectively, these observations suggest that MEMO1 facilitates the replacement of terminally differentiated chondrocytes by ossified bone in the cranial base, potentially through regulating vascular development.

In what germ layers, tissues, and cell types does MEMO1 function during cranial base ossification? Using the *LacZ* reporter allele to track *Memo1* expression, we found most robust β-galactosidase activity in the perichondrium and periosteum of the chondrocranium. Less prominent β-galactosidase staining was observed in various zones of chondrocyte maturation, including resting, proliferative, and hypertrophic chondrocytes. In addition, punctate β-galactosidase activity was observed within developing bones of the cranial base (as well as intramembranous bones, such as the maxillary and palatine bone). These findings suggested that MEMO1 could function in multiple components of the developing cranial base. Therefore, we have employed Cre-recombinase mediated deletion of *Memo1* to begin probing the tissue specific role of this gene in craniofacial development. Focusing on the neural crest, we have determined that MEMO1 has an autonomous role within this tissue during cranial base ossification, as the most anterior element, the presphenoid, failed to

ossify. Given that neural crest cells supply the undifferentiated mesenchyme of the anterior cranial base [7], and thus all tissues of the cartilage anlage, the supporting perichondrium and periosteum, and bone forming cells (osteoblasts), MEMO1's role is likely autonomous to one of these cell types. In this context, it is important to consider the complex interplay of mesoderm and neural crest cells in development of the cranial base. Thus, both the cartilage and bone of the presphenoid are neural crest cell-derived, whereas the basioccipital cartilage and bone is derived entirely from the somitic mesoderm. Between these elements, the basisphenoid has a more complex origin, with the cartilage anlage of the basisphenoid bone mainly neural crest cell-derived, whereas the bone originates from cranial paraxial mesoderm [7-9]. Importantly, following neural crest cell-specific deletion of *Memo1* the basisphenoid bone is relatively unperturbed, especially in comparison to the full null, where it is hypoplastic. This finding suggests that any defects in the neural crest cell-derived cartilage can be at least partially rescued if the bone (i.e. osteoblasts) itself is derived from the mesoderm and further supports a prominent role for MEMO1 at a "post-cartilage development" stage. Moreover, we note that additional bones of the cranial base can form normally in the neural crest cell-conditional mutant compared with the *Memo1*-null. Thus, the presence of bones derived from the hypochiasmatic cartilages in the conditional deletion, but not the null, highlights the mesodermal origin of these elements and further indicates that MEMO1 presumably functions in the mesoderm to regulate their ossification. In the future, tissue-specific deletion of *Memo1* in additional domains should pinpoint the critical tissues/cell types in which this gene might function during cranial base ossification, including the mesoderm, cartilage, osteoblasts, and perichondrium. It is also possible that MEMO1 could function in the blood vessels associated with the developing cranial base, especially given the apparent vasculature defects observed when *Memo1* is lost on the 129S1/SvImJ background [22]. Indeed, the neural crest cells are known to provide pericytes to the craniofacial vasculature [58]. However, we do not favor this possibility as previous studies targeting *Memo1* with the endothelial-specific Tie2-Cre frequently resulted in mice that were viable in the post-natal period [22], implying that primary defects in the endothelial component of the vasculature is not a major source of the embryonic lethality associated with the craniofacial defects we observed in our neural crest-specific conditional mutants.

What is the function of MEMO1 in driving cranial base ossification? Based on previous roles identified for MEMO1 as well as the findings presented here, there are a variety of non-mutually exclusive models for how MEMO1 may drive ossification of the cranial base. First, MEMO1 may facilitate signaling downstream of an RTK during cranial base ossification. Specifically, analyses in other physiological and developmental processes have shown that MEMO1 mediates signaling downstream of a variety of RTKs, including ERBB2 [19,59], EGFR [19], FGFR [19,27], IGF1R [59], and PDGFR [22]. Interestingly, previous work has also identified a role for these signaling pathways, including their effectors such as ERK1/2, in driving endochondral ossification, either in the cranial base directly or other endochondral bones [60-65]. VEGFR1 (Flt1) and/or VEGFR2 (Flk1) are also excellent RTK candidates that might function in concert with MEMO1 as disruption to VEGF signaling results in reduced ossification associated with decreased vascularity and an elongated hypertrophic zone, similar to *Memo1* mutants [66-68]. In addition, MEMO1 has been shown to interact with and influence downstream signaling from the estrogen receptor, another key

pathway essential for bone development and homeostasis [59,69]. Thus, one possibility is that the loss of MEMO1 would uncouple one or more RTKs or signaling pathways from its downstream function in driving ossification. In turn, lost or reduced signaling could ultimately lead to a reduction in expression of cartilage to bone promoting factors, such as MMP9 and MMP13, as has been described during ossification in EGFR mutants [70]. A second plausible model for how MEMO1 may promote ossification is through its ability to generate ROS, a recently identified biochemical function for MEMO1 in other contexts [21], and a known mechanism driving endochondral ossification [71-73]. ROS production during endochondral ossification has been shown to promote chondrocyte maturation and eventual apoptosis during bone replacement [71-73]. In addition, ROS has been shown to drive mRNA expression of pro-osteogenic *Mmp13* in chondrocytes [74], a gene which was also significantly down-regulated in the cranial base of *Memo1* mutants. Physiological levels of ROS are also required for appropriate vasculogenesis, and alterations in ROS production could conceivably impact the distribution of blood vessels in the cranial base. Therefore, the loss of MEMO1 function in ROS production would affect many of the physiological pathways required for normal endochondral ossification. Future studies will be needed to address the biochemical function(s) of MEMO1 that is critical in regulating endochondral ossification.

Another major defect evident in *Memo1* mutants is clefting of the secondary palate. MEMO1's role during overt palatal closure largely appears to be extrinsic to this structure based on the following observations. First, despite a failure in palatal shelf elevation in *Memo1* mutants, thorough analysis of the palate identified few molecular changes. Second, MEMO1 was only expressed at a moderate level within the palatal shelf mesenchyme directly, especially by E15.5. Third, conditional deletion of MEMO1 from neural crest cells, in the majority of cases, failed to recapitulate the cleft palate phenotype as seen in *Memo1* null embryos. As such, palatal bones (maxillary and palatine) were less affected in conditional mutants, despite their neural crest cell origin [11,13,23]. Preliminary data also show that loss of *Memo1* in the ectoderm of the palatal shelves does not cause an overt clefting phenotype (EVO, unpublished observations). Taken together, these findings suggest that the overt cleft palate phenotype may be secondary to primary defects in other tissues, including the cranial base. However, additional testing will be required to test the validity of this model. It is important to note that conditional mutants still presented with pathological defects of the secondary palate, although these were milder than those seen in the null. Specifically, neural crest cell-specific deletion of *Memo1* resulted in hypoplastic development of the palatal process of both the maxillary and palatine bones, consistent with a submucosal cleft palate. Importantly, there are currently few mouse models for this common type of human palatal defect but a submucosal cleft palate is present in *Tbx22* mouse mutants, responsible for X-linked cleft palate and ankyloglossia in humans. Notably, these *Tbx22* mutants die at birth due to an inability to suckle [75] similar to *Memo1* neural crest conditional mutants. Future studies will need to address the full extent of MEMO1's role during palatogenesis and suckling as well as how structures such as the cranial base and tongue – potentially via defects in hyoid ossification - may be influencing these events. Note that defects in the cranial base would provide an additional mechanism by which closure of the palate could be linked with abnormalities in an extrinsic developmental process,

alongside a failure of descent of the tongue, as has previously been described [76]. Teasing out these developmental relationships will be critical as cranial base defects have been associated with a variety of craniofacial anomalies, including isolated cleft palate. Indeed, the hypothesis that alterations in human cranial base morphology can affect development and clefting of the secondary palate has been the subject of much debate, and our studies provide strong support for such a mechanistic connection [4-6,77-80].

Finally, identification of MEMO1 as a novel effector of both ossification and palatal development implicates it as a potential component of human congenital disorders affecting palatogenesis and/or osteogenesis. To date, no mutations in *MEMO1* have been identified in human orofacial clefting, although a case-parent trio study examining candidate genes for non-syndromic cleft palate, which focused on chromosome 2, identified evidence of linkage disequilibrium (LD) for markers located in *SLC30A6* [81]. Interestingly, *SLC30A6* is located 50-100Kb from *MEMO1* (separated only by the genes *SPAST* and *DPY30*), raising the possibility that significant LD is a result of *MEMO1*, or *MEMO1 cis*-regulatory elements, in affected individuals. In the context of human osteogenic conditions, multiple studies on patients with low bone mineral density find significant linkage to chromosome 2p23-24, a locus that includes *MEMO1* [82-84]. It is also interesting to note that cranial base anomalies are an important complication of osteogenesis imperfect (OI), associated with mutations in *COL1A1, COL1A2*, and *SP7*, and both *Col1a2* and *Sp7* are significantly down-regulated in the cranial base of *Memo1* mutants [85-88]. In conclusion, our findings suggest that MEMO1 is part of the regulatory hierarchy controlling the timing of cranial base ossification and palate formation. Thus, we predict that a reduction in human MEMO1 function would lead to the types of cranial base defects observed in OI, such as platybasia, and potentially cleft palate. Alternatively, an increase in MEMO1 activity would lead to premature fusion of the cranial base synchondroses and with associated defects in growth of the face and calvaria. Our studies, therefore suggest that MEMO1 be considered in the pathology related to disorders of ossification, in particular those affecting the cranial base, as well as in palatal clefting.

Materials and Methods

Mice

Male C57BL/6J mice treated with ENU were kindly provided by Monica Justice (Baylor College of Medicine, Houston, Texas, now at The Hospital for Sick Children [SickKids] in Toronto, Ontario). Additional C57BL/6J mice and 129S1/SvImJ mice were obtained from the Jackson Laboratory (Bar Harbor, ME). Wnt1-CRE mice were previously reported and obtained from Jackson Laboratory [33]. The rosa-Tomato mouse strain was also previously reported and was a kind gift from the lab of Linda Barlow (University of Colorado - Denver, Aurora, CO) [34]. This study was carried out in strict accordance with the recommendations in the Guide for the Care and Use of Laboratory Animals of the National Institutes of Health. The protocol was approved by the Institutional Animal Care and Use Committee of the University of Colorado Denver. Noon on the day a copulatory plug was present was denoted as embryonic day 0.5. Yolk sacs or tail clips were used for genotyping. DNA for PCR was extracted using DirectPCR Lysis Reagent (Viagen Biotech. Inc, Los Angeles, CA) plus

10ug/ml Proteinase K (Roche, Basel, Switzerland) followed by heat inactivation at 85°C for 45 mins. Samples were then used directly for PCR-based genotyping using the primers listed in Supplemental Table 2 at a concentration of 200 nM using the Qiagen DNA polymerase kit, including the optional Q Buffer solution (Qiagen, Valencia, CA). XmnI used for further analysis of PCR products was obtained from New England Biolabs (Ipswich, MA).

Skeletal analysis

Bone and cartilage staining

Embryos were collected at appropriate time points and processed as previously described [89]. Briefly, following euthanasia, skin and organs were removed and embryos were dehydrated in 95% ethanol until further processing. Subsequently, embryos were incubated in acetone (~2 days) followed by incubation in a solution of acetic acid (5%) and 70% ethanol containing alcian blue (0.3%), and alizarin red (0.1%), for 2-3 days with shaking at 37°C, for staining of bone and cartilage elements. Following staining, remaining soft tissue was dissolved in 2% KOH (~1-2 days) and then 1% KOH (~1-2 days) until properly cleared. Final skeletal preparations were stored at 4°C in 25% glycerol and 1% KOH.

Cartilage staining

Embryos were collected at appropriate time points and processed as previously described [90]. Briefly, following euthanasia, embryos were fixed in Bouin's solution at 4°C overnight. Following fixation, embryos were washed with repeated changes of a solution of 70% ethanol and 0.1% NH_4OH, until all traces of Bouin's were removed. Subsequently, tissue was permeabilized by two 1 hour washes in 5% acetic acid, followed by overnight incubation in a solution of alcian blue (0.05%) and acetic acid (5%). Following staining, embryos were washed twice with 5% acetic acid (~1hr each wash) and then twice with 100% MeOH (~1hr each wash). Finally, embryos were cleared with a solution consisting of one part benzyl alcohol and two parts benzyl benzoate (BABB).

Mapping and Exome sequencing

Meiotic mapping to localize the ENU mutation responsible for the F1-9-13FP phenotype was performed as previously described [91,92]. Subsequently, mutations within this interval were identified by sequencing F1-9-13FP homozygous mutant genomic DNA using the NimbleGen Mouse Exome Capture Kit followed by HiSeq2000 NextGen sequencing with >30x coverage (Otogenetics Corporation, Norcross, GA). Following sequencing, reads were mapped to the reference mouse genome sequence (Mm9) with large-scale alignment software (gSNAP). Sequence calls for single-nucleotide polymorphisms were performed using the Broad's Genome Analysis Toolkit (GATK). The resulting variants were filtered in a systematic way to further reduce false positive results. Subsequently, the program ANNOVAR was used to cross reference all the variants across several genetic variation databases (e.g., dbSNP, AVSIFT, etc.) to find those variants that were likely to be novel. Variants considered as putative mutations after data filtering and analysis were 'reconfirmed' with custom designed Sanger Sequencing methods.

Western blot analysis

For Western blot analysis, E13.5 embryonic heads were lysed in RIPA buffer containing protease inhibitors (Thermo Scientific™ Protease Inhibitor Cocktail, Thermo Scientific, Waltham, MA). Briefly, heads were first minced using a razor blade followed by further disruption using a tissue homogenizer (Pro200 homogenizer, PRO Scientific Inc, Oxford, CT). Following homogenization, samples were allowed to lyse on ice for ~30 minutes. After lysis, 6x Laemmli Buffer (plus β-mercaptoethanol) was added to 1x final concentration and samples stored at −80°C until use. On the day of use, samples were boiled at ~100°C for 10 minutes, spun at 13,000 rpm for 10 minutes, and then 30uL of lysate loaded per lane on a 12% stacking polyacrylamide gel and run at 100V. Once samples were resolved, they were transferred onto a nitrocellulose membrane overnight at 4°C at 40mA. Following transfer, membranes were blocked one hour with 3% powdered milk in TBST (TBSTM), and then incubated with the primary antibody, diluted in TBSTM, overnight at 4°C (anti-MEMO1, 1:1000) [21]. Following primary antibody incubation, membranes were washed 4x20min with TBSTM and then incubated with an infrared (IR)-labeled secondary antibody for 1hr (1:20,000 in TBST, LI-COR Biosciences, Lincoln, NE). The membrane was then washed 4x20min with TBSTM, 5 min with PBS, and then imaged on a LI-COR Odyssey imager. Following imaging, as a loading control, an additional primary antibody was added to the membrane (anti-ACTIN, H-196, 1:1000, Santa Cruz Biotechnology, Inc., Dallas, TX) and a similar washing, secondary, and imaging procedure carried out.

EUCOMM alleles - ES cells, injection, chimera generation, breeding, genotyping

To generate the *Memo1* null allele we obtained ES-cells (*Memo1*$^{tm1a(EUCOMM)Wtsi}$) from the European Conditional Mouse Mutagenesis (EUCOMM) repository that harbored a “targeted trap” allele at the *Memo1* locus, generated on the C57BL/6N background (this allele includes an inserted *LacZ* and *neomycin* selection cassette, downstream of a strong splice-acceptor, as well as loxP sites flanking exon 4 of *Memo1*, see Supplemental Fig 2A) [26]. Using standard procedures, chimeric mice were generated using these ES-cells, and subsequently bred with outbred wild-type Black Swiss mice to obtain germ-line transmission, establishing a heterozygous line (EUCOMM *tm1a* allele, this allele referred to as *Memo1*^{neo}, confirmed by PCR, see Supplemental Fig 2A). Subsequently, to generate a “null-allele” these mice were bred with mice harboring CRE-recombinase expressed ubiquitously under control of an *Actin* promoter [93], resulting in deletion of the *neo*-cassette as well as exon 4 of *Memo1* in 25% of the generated offspring (although the *LacZ*-cassette was retained, EUCOMM *tm1b* allele, referred to as *Memo1 knock-in, or Memo1*^{ki}, see Supplemental Fig 2C). The deletion of exon 4 in a subset of the offspring was confirmed by PCR from genomic DNA, followed by sequencing (Supplemental Fig 2C and not shown). The conditional allele was generated by breeding mice harboring the *Memo1*^{neo} allele with mice ubiquitously expressing FLPe recombinase [94]. Acquisition of both alleles in the generated offspring resulted in FLPe mediated excision of the *LacZ-neomycin* selection cassette, resulting in loxP sites flanking exon 4 of *Memo1* (EUCOMM *tm1c* allele, referred to as *Memo1*^{flp}, see Supplemental Fig 2B), confirmed by PCR. Once generated, alleles were maintained on the C57BL/6J background. All primers used for genotyping are listed in Supplemental Table 2.

In situ hybridization/Immunohistochemistry/Immunofluorescence/H&E staining

In situ hybridization was carried out essentially as previously described [95]. For all probes listed, with the exception of *Hoxa2* (a kind gift from Robb Krumlauf) [32], a unique fragment (primer sequences given upon request) was cloned into a TOPO vector (Life Technologies, Grand Island, NY), using cDNA synthesized from mouse embryonic mRNA, as a template. cDNA was generated using the SuperScript® III First-Strand Synthesis System (Life Technologies, Grand Island, NY), as per manufacturer's instructions. Sequence verified plasmids were linearized and antisense probes synthesized using an appropriate DNA-dependent RNA polymerase (T7/T3/SP6) and DIG RNA labeling mix (Roche, Basel, Switzerland).

Whole-mount immunohistochemistry was carried out essentially as described, replacing 10% horse serum with 5% milk as a blocking reagent [96]. The anti-neurofilament antibody [97] was used at a 1:100 dilution (IgG clone 2H3, obtained from the Developmental Studies Hybridoma Bank, created by the NICHD of the NIH and maintained at The University of Iowa, Department of Biology, Iowa City, IA).

Section Immunofluorescence: Dissected samples were fixed overnight in 4% paraformaldehyde (PFA). Subsequent to genotyping, samples were taken through a series of 30% sucrose, 30% sucrose/50% OCT (Tissue-Tek® O.C.T. Compound, Electron Microscopy Sciences, Hatfield, PA), and 100% OCT, and frozen on dry ice. Sections were cut at 10μm on a Leica CM 1900 cryostat (Leica Biosystems Inc., Buffalo Grove, IL) and placed on charged slides. Post-sectioning, samples were processed using the M.O.M. kit (Vector Laboratories, Inc., Burlingame, CA), as per manufacturer's instructions, with the following exceptions: H_2O_2 treatment and antigen retrieval were omitted and a fluorescent secondary antibody used in place of colorimetric detection. Following primary antibody incubation (CD31, IgG clone 2H8, 1:100) [57], samples were rinsed 2×10 min with PBS, and then incubated with a fluorescent secondary antibody (goat-anti-mouse 594) (Invitrogen, Carlsbad, CA) along with the nuclear counterstain, DRAQ5 (Abcam, Cambridge, UK), for ~30 min. Following this incubation, samples were rinsed 2×10 min in PBS and cover-slipped. For older staged embryos (E18.5), samples were first decalcified in 10% EDTA for ~5 days post-fixation, prior to embedding in sucrose and OCT.

Hematoxylin and Eosin (H&E) staining was carried out essentially as previously described [98]. Briefly, samples were fixed overnight in 4% PFA. Following fixation, tissue was dehydrated in a graded series of ethanol and xylene and subsequently embedded in paraffin. After embedding, samples were sectioned with a Leica RM 2235 microtome at 10uM, onto charged glass slides. After drying, sections were processed for H&E staining using standard procedures.

β-galactosidase staining

β-galactosidase staining of frozen sections was carried out as previously described [99]. Briefly, dissected samples were fixed for 30 minutes in 0.2% glutaraldehyde, soaked in 10%

sucrose in PBS for 30 minutes, then PBS plus 2mM $MgCl_2$, followed by 30% sucrose/50% OCT /2mM $MgCl_2$ for at least two hours. Subsequently, tissue was embedded in OCT on dry-ice. Sections were cut at 10uM and mounted on charged glass slides. Following sectioning, samples were fixed in 0.2% glutaraldehyde for 10 minutes on ice, rinsed with 2mM $MgCl_2$ in PBS, incubated in 2mM $MgCl_2$ in PBS for 10 minutes on ice, incubated in detergent rinse solution (0.005% NP40, 0.01% sodium deoxycholate in PBS) for 10 minutes on ice, and then developed in *LacZ* staining solution (detergent rinse solution plus 1mg/ml X-Gal, Invitrogen/Life Technologies, Carlsbad, CA) at room temperature for two days in the dark. Following staining, sections were counterstained with Nuclear Fast Red (Vector Laboratories, Inc., Burlingame, CA).

Cell proliferation and cell death analysis

For EdU staining, staged pregnant mice were injected intraperitoneally with 150uL of 1mg/ml EdU in PBS, using the Click-iT® EdU Alexa Fluor® 594 Imaging Kit (Life Technologies/ThermoFisher Scientific). Approximately 1 hour later, embryos were removed and fixed in 4% PFA overnight at 4°C. Following fixation, tissue was dehydrated in a graded series of ethanol and xylene and subsequently embedded in paraffin. After embedding, samples were sectioned with a Leica RM 2235 microtome at 10uM, onto charged glass slides. After drying, sections were processed for EdU immunofluorescence as per manufacturer's instructions and subsequently counterstained with DRAQ5 in PBS (1:1000). Processed samples were imaged on a Leica TCS SP5 II confocal microscope and individual images taken for quantification. Images were scored blindly for both total cell number (DRAQ5+ cells) and total proliferative cell number (EdU+ cells) using the cell counting plugin for ImageJ [100], and percentage of proliferating cells calculated. Mean and standard deviation were calculated between groups and a standard Student’s t-test was used for calculating p-value. Analysis of cell death was carried out using the DeadEnd™ Fluorometric TUNEL System, as per manufacturer's instructions (Promega, Madison, WI).

RNAseq

For the palatal RNA-seq, E13.5 embryos, generated from a $Memo1^{wt/m1Will}$ in-cross (on a largely C57 background, >95%), were dissected in ice-cold PBS. Subsequently, palatal shelves were carefully dissected from each embryo and stored in RNAlater (Ambion/Life Technologies) until later use. Following genotyping, RNA was extracted from both palatal shelves (3 control and 3 mutant embryos = 6 palatal shelves/group) using the microRNA Purification Kit (Norgen Biotek Corp., Thorold, ON), following manufacturer's protocol.

Following elution, mRNA was further purified using the Qiagen RNAeasy Kit (Qiagen, Valencia, CA), according to manufacturer's protocol. Quality of extracted mRNA was assessed using DNA Analysis ScreenTape (Agilent Technologies, Santa Clara, CA) to ensure that it was of sufficient quality for library production. Following validation of extracted mRNA, cDNA libraries were generated using the Illumina TruSeq Stranded mRNA Sample Prep Kit (Illumina, San Diego, CA). Following library generation and subsequent quality control assessment, cDNA was sequenced using the Illumina HiSeq2500 platform and single-end reads (1x50). For RNAseq of cranial base samples, a similar approach was used, with the exception that E15.5 embryos were used and the cranial base

processed rather than the palatal shelves. For functional annotation clustering of significantly upregulated and downregulated genes, DAVID [35], with default parameters, was used. Following functional annotation clustering, “annotation clusters” above a 2-fold enrichment threshold were considered.

Supplementary Material

Refer to Web version on PubMed Central for supplementary material.

Acknowledgements

This work supported by Fellowship F32DE02370 from the National Institute of Dental and Craniofacial Research (EVO), in part by a Cleft Palate Foundation Research Support Grant (EVO) and an American Association of Anatomists Postdoctoral Fellowship (EVO); Grants R01 DE019843 and R01 HD081562 (TW); SNF 310030A-121574 and 310030B-138674 (NEH); and Department of Pediatrics, Children’s Hospital Colorado (LN, for ENU screen). LN was an investigator of the Howard Hughes Medical Institute. Bioinformatic analyses were supported in part by the Biostatistics/Bioinformatics Shared Resources of Colorado's NIH/NCI Cancer Center (support grant P30CA046934). We thank the Genomics and Microarray Core at UC-Denver for their assistance in RNA-seq experiments, Philip O’Neill (UC-Denver, Aurora, CO) for help in processing of RNA-seq data, Timothy P Nottoli (Yale University, New Haven, CT) for blastocyst injections, Monica Justice (originally Baylor College of Medicine, Houston, Texas, now at The Hospital for Sick Children [SickKids] in Toronto, Ontario) for initially supplying the ENU mutagenized sperm used in the recessive screen, and Irene Choi (UC-Denver, Aurora, CO) for mouse maintenance and DNA extraction from ENU mutants.

References

1. Lieberman DE, Pearson OM, Mowbray KM. Basicranial influence on overall cranial shape. Journal of human evolution. 2000; 38:291–315. doi:10.1006/jhev.1999.0335. [PubMed: 10656780]
2. Lieberman DE, Ross CF, Ravosa MJ. The primate cranial base: ontogeny, function, and integration. American journal of physical anthropology. 2000; Suppl 31:117–169. [PubMed: 11123839]
3. Martinez-Abadias N, et al. Pervasive genetic integration directs the evolution of human skull shape. Evolution; international journal of organic evolution. 2012; 66:1010–1023. doi:10.1111/j.1558-5646.2011.01496.x.
4. Nie X. Cranial base in craniofacial development: developmental features, influence on facial growth, anomaly, and molecular basis. Acta odontologica Scandinavica. 2005; 63:127–135. doi:10.1080/00016350510019847. [PubMed: 16191905]
5. Jahanbin A, Eslami N, Hoseini Zarch H, Kobravi S. Comparative evaluation of cranial base and facial morphology of cleft lip and palate patients with normal individuals in cone beam computed tomography. The Journal of craniofacial surgery. 2015; 26:785–788. doi:10.1097/SCS.0000000000001361. [PubMed: 25915676]
6. Ye B, et al. A comparative cephalometric study for adult operated cleft palate and unoperated cleft palate patients. Journal of cranio-maxillo-facial surgery : official publication of the European Association for Cranio-Maxillo-Facial Surgery. 2015 doi:10.1016/j.jcms.2015.04.015.
7. McBratney-Owen B, Iseki S, Bamforth SD, Olsen BR, Morriss-Kay GM. Development and tissue origins of the mammalian cranial base. Developmental biology. 2008; 322:121–132. doi:10.1016/j.ydbio.2008.07.016. [PubMed: 18680740]
8. Couly GF, Coltey PM, Le Douarin NM. The triple origin of skull in higher vertebrates: a study in quail-chick chimeras. Development. 1993; 117:409–429. [PubMed: 8330517]
9. Le Douarin, N.; Kalcheim, C. The neural crest. 2nd. Cambridge University Press; 1999.
10. Gross JB, Hanken J. Review of fate-mapping studies of osteogenic cranial neural crest in vertebrates. Developmental biology. 2008; 317:389–400. doi:10.1016/j.ydbio.2008.02.046. [PubMed: 18402934]
11. Jiang X, Iseki S, Maxson RE, Sucov HM, Morriss-Kay GM. Tissue origins and interactions in the mammalian skull vault. Developmental biology. 2002; 241:106–116. doi:10.1006/dbio.2001.0487. [PubMed: 11784098]

12. Percival CJ, Richtsmeier JT. Angiogenesis and intramembranous osteogenesis. Developmental dynamics : an official publication of the American Association of Anatomists. 2013; 242:909–922. doi:10.1002/dvdy.23992. [PubMed: 23737393]
13. Rossant J, Tam PPL. Mouse development : patterning, morphogenesis, and organogenesis. 2002 Academic.
14. Yang Y. Skeletal morphogenesis during embryonic development. Critical reviews in eukaryotic gene expression. 2009; 19:197–218. [PubMed: 19883365]
15. Franz-Odendaal TA. Induction and patterning of intramembranous bone. Frontiers in bioscience. 2011; 16:2734–2746.
16. Hayashi S, et al. Interface between intramembranous and endochondral ossification in human foetuses. Folia morphologica. 2014; 73:199–205. doi:10.5603/FM.2014.0029. [PubMed: 24902099]
17. Chung UI, Kawaguchi H, Takato T, Nakamura K. Distinct osteogenic mechanisms of bones of distinct origins. Journal of orthopaedic science : official journal of the Japanese Orthopaedic Association. 2004; 9:410–414. doi:10.1007/s00776-004-0786-3. [PubMed: 15278782]
18. Feng W, Choi I, Clouthier DE, Niswander L, Williams T. The Ptch1(DL) mouse: a new model to study lambdoid craniosynostosis and basal cell nevus syndrome-associated skeletal defects. Genesis. 2013; 51:677–689. doi:10.1002/dvg.22416. [PubMed: 23897749]
19. Marone R, et al. Memo mediates ErbB2-driven cell motility. Nature cell biology. 2004; 6:515–522. doi:10.1038/ncb1134. [PubMed: 15156151]
20. Meira M, et al. Memo is a cofilin-interacting protein that influences PLCgamma1 and cofilin activities, and is essential for maintaining directionality during ErbB2-induced tumor-cell migration. Journal of cell science. 2009; 122:787–797. doi:10.1242/jcs.032094. [PubMed: 19223396]
21. MacDonald G, et al. Memo is a copper-dependent redox protein with an essential role in migration and metastasis. Science signaling. 2014; 7:ra56. doi:10.1126/scisignal.2004870. [PubMed: 24917593]
22. Kondo S, et al. Memo has a novel role in S1P signaling and is [corrected] crucial for vascular development. PloS one. 2014; 9:e94114. doi:10.1371/journal.pone.0094114. [PubMed: 24714781]
23. Noden DM, Trainor PA. Relations and interactions between cranial mesoderm and neural crest populations. Journal of anatomy. 2005; 207:575–601. doi:10.1111/j.1469-7580.2005.00473.x. [PubMed: 16313393]
24. Thompson H, Ohazama A, Sharpe PT, Tucker AS. The origin of the stapes and relationship to the otic capsule and oval window. Developmental dynamics : an official publication of the American Association of Anatomists. 2012; 241:1396–1404. doi:10.1002/dvdy.23831. [PubMed: 22778034]
25. Weir M, Rice M. Ordered partitioning reveals extended splice-site consensus information. Genome Res. 2004; 14:67–78. doi:10.1101/gr.1715204. [PubMed: 14707171]
26. Skarnes WC, et al. A conditional knockout resource for the genome-wide study of mouse gene function. Nature. 2011; 474:337–342. doi:10.1038/nature10163. [PubMed: 21677750]
27. Haenzi B, et al. Loss of Memo, a novel FGFR regulator, results in reduced lifespan. FASEB journal : official publication of the Federation of American Societies for Experimental Biology. 2014; 28:327–336. doi:10.1096/fj.13-228320. [PubMed: 24056085]
28. Zaoui K, Honore S, Isnardon D, Braguer D, Badache A. Memo-RhoA-mDia1 signaling controls microtubules, the actin network, and adhesion site formation in migrating cells. The Journal of cell biology. 2008; 183:401–408. doi:10.1083/jcb.200805107. [PubMed: 18955552]
29. Zhang J, et al. Neural tube, skeletal and body wall defects in mice lacking transcription factor AP-2. Nature. 1996; 381:238–241. doi:10.1038/381238a0. [PubMed: 8622766]
30. Mitchell PJ, Timmons PM, Hebert JM, Rigby PW, Tjian R. Transcription factor AP-2 is expressed in neural crest cell lineages during mouse embryogenesis. Genes & development. 1991; 5:105–119. [PubMed: 1989904]
31. Reid BS, Sargent TD, Williams T. Generation and characterization of a novel neural crest marker allele, Inka1-LacZ, reveals a role for Inka1 in mouse neural tube closure. Developmental dynamics : an official publication of the American Association of Anatomists. 2010; 239:1188–1196. doi:10.1002/dvdy.22248. [PubMed: 20175189]

32. Wilkinson DG, Bhatt S, Cook M, Boncinelli E, Krumlauf R. Segmental expression of Hox-2 homoeobox-containing genes in the developing mouse hindbrain. Nature. 1989; 341:405–409. doi: 10.1038/341405a0. [PubMed: 2571936]
33. Danielian PS, Muccino D, Rowitch DH, Michael SK, McMahon AP. Modification of gene activity in mouse embryos in utero by a tamoxifen-inducible form of Cre recombinase. Current biology : CB. 1998; 8:1323–1326. [PubMed: 9843687]
34. Madisen L, et al. A robust and high-throughput Cre reporting and characterization system for the whole mouse brain. Nature neuroscience. 2010; 13:133–140. doi:10.1038/nn.2467. [PubMed: 20023653]
35. Huang da W, et al. Extracting biological meaning from large gene lists with DAVID. Current protocols in bioinformatics / editoral board, Andreas D. Baxevanis … [et al.]. 2009 Chapter 13, Unit 13 11. doi:10.1002/0471250953.bi1311s27.
36. Vu TH, et al. MMP-9/gelatinase B is a key regulator of growth plate angiogenesis and apoptosis of hypertrophic chondrocytes. Cell. 1998; 93:411–422. [PubMed: 9590175]
37. Inada M, et al. Critical roles for collagenase-3 (Mmp13) in development of growth plate cartilage and in endochondral ossification. Proceedings of the National Academy of Sciences of the United States of America. 2004; 101:17192–17197. doi:10.1073/pnas.0407788101. [PubMed: 15563592]
38. Stickens D, et al. Altered endochondral bone development in matrix metalloproteinase 13-deficient mice. Development. 2004; 131:5883–5895. doi:10.1242/dev.01461. [PubMed: 15539485]
39. Gustafsson E, et al. Role of collagen type II and perlecan in skeletal development. Annals of the New York Academy of Sciences. 2003; 995:140–150. [PubMed: 12814946]
40. Hayman AR, et al. Mice lacking tartrate-resistant acid phosphatase (Acp 5) have disrupted endochondral ossification and mild osteopetrosis. Development. 1996; 122:3151–3162. [PubMed: 8898228]
41. Holm E, Aubin JE, Hunter GK, Beier F, Goldberg HA. Loss of bone sialoprotein leads to impaired endochondral bone development and mineralization. Bone. 2015; 71:145–154. doi:10.1016/j.bone. 2014.10.007. [PubMed: 25464126]
42. Padovano JD, Ramachandran A, Bahmanyar S, Ravindran S, George A. Bone-specific overexpression of DMP1 influences osteogenic gene expression during endochondral and intramembranous ossification. Connective tissue research. 2014; 55 Suppl 1:121–124. doi: 10.3109/03008207.2014.923878. [PubMed: 25158195]
43. Bouet G, et al. The impairment of osteogenesis in bone sialoprotein (BSP) knockout calvaria cell cultures is cell density dependent. PloS one. 2015; 10:e0117402. doi:10.1371/journal.pone. 0117402. [PubMed: 25710686]
44. Nakashima K, et al. The novel zinc finger-containing transcription factor osterix is required for osteoblast differentiation and bone formation. Cell. 2002; 108:17–29. [PubMed: 11792318]
45. Chipman SD, et al. Defective pro alpha 2(I) collagen synthesis in a recessive mutation in mice: a model of human osteogenesis imperfecta. Proceedings of the National Academy of Sciences of the United States of America. 1993; 90:1701–1705. [PubMed: 8446583]
46. Kawai S, Yamauchi M, Wakisaka S, Ooshima T, Amano A. Zinc-finger transcription factor odd-skipped related 2 is one of the regulators in osteoblast proliferation and bone formation. Journal of bone and mineral research : the official journal of the American Society for Bone and Mineral Research. 2007; 22:1362–1372. doi:10.1359/jbmr.070602.
47. St-Jacques B, Hammerschmidt M, McMahon AP. Indian hedgehog signaling regulates proliferation and differentiation of chondrocytes and is essential for bone formation. Genes & development. 1999; 13:2072–2086. [PubMed: 10465785]
48. Deng C, Wynshaw-Boris A, Zhou F, Kuo A, Leder P. Fibroblast growth factor receptor 3 is a negative regulator of bone growth. Cell. 1996; 84:911–921. [PubMed: 8601314]
49. Wiedemann M, Trueb B. Characterization of a novel protein (FGFRL1) from human cartilage related to FGF receptors. Genomics. 2000; 69:275–279. doi:10.1006/geno.2000.6332. [PubMed: 11031111]
50. Akiyama H, Chaboissier MC, Martin JF, Schedl A, de Crombrugghe B. The transcription factor Sox9 has essential roles in successive steps of the chondrocyte differentiation pathway and is

required for expression of Sox5 and Sox6. Genes & development. 2002; 16:2813–2828. doi: 10.1101/gad.1017802. [PubMed: 12414734]

51. Watanabe H, et al. Mouse cartilage matrix deficiency (cmd) caused by a 7 bp deletion in the aggrecan gene. Nature genetics. 1994; 7:154–157. doi:10.1038/ng0694-154. [PubMed: 7920633]
52. Li SW, et al. Transgenic mice with targeted inactivation of the Col2 alpha 1 gene for collagen II develop a skeleton with membranous and periosteal bone but no endochondral bone. Genes & development. 1995; 9:2821–2830. [PubMed: 7590256]
53. Fassler R, et al. Mice lacking alpha 1 (IX) collagen develop noninflammatory degenerative joint disease. Proceedings of the National Academy of Sciences of the United States of America. 1994; 91:5070–5074. [PubMed: 8197187]
54. Nakamichi Y, et al. Chondromodulin I is a bone remodeling factor. Molecular and cellular biology. 2003; 23:636–644. [PubMed: 12509461]
55. Ortega N, Behonick D, Stickens D, Werb Z. How proteases regulate bone morphogenesis. Annals of the New York Academy of Sciences. 2003; 995:109–116. [PubMed: 12814943]
56. Ortega N, Behonick DJ, Werb Z. Matrix remodeling during endochondral ossification. Trends in cell biology. 2004; 14:86–93. doi:10.1016/j.tcb.2003.12.003. [PubMed: 15102440]
57. Bogen SA, Baldwin HS, Watkins SC, Albelda SM, Abbas AK. Association of murine CD31 with transmigrating lymphocytes following antigenic stimulation. The American journal of pathology. 1992; 141:843–854. [PubMed: 1415479]
58. Etchevers HC, Vincent C, Le Douarin NM, Couly GF. The cephalic neural crest provides pericytes and smooth muscle cells to all blood vessels of the face and forebrain. Development. 2001; 128:1059–1068. [PubMed: 11245571]
59. Jiang K, et al. Mediator of ERBB2-driven cell motility (MEMO) promotes extranuclear estrogen receptor signaling involving the growth factor receptors IGF1R and ERBB2. The Journal of biological chemistry. 2013; 288:24590–24599. doi:10.1074/jbc.M113.467837. [PubMed: 23861392]
60. Fisher MC, Clinton GM, Maihle NJ, Dealy CN. Requirement for ErbB2/ErbB signaling in developing cartilage and bone. Development, growth & differentiation. 2007; 49:503–513. doi: 10.1111/j.1440-169X.2007.00941.x.
61. Britto JA, Evans RD, Hayward RD, Jones BM. From genotype to phenotype: the differential expression of FGF, FGFR, and TGFbeta genes characterizes human cranioskeletal development and reflects clinical presentation in FGFR syndromes. Plastic and reconstructive surgery. 2001; 108:2026–2039. discussion 2040-2026. [PubMed: 11743396]
62. Rice DP, Rice R, Thesleff I. Fgfr mRNA isoforms in craniofacial bone development. Bone. 2003; 33:14–27. [PubMed: 12919696]
63. Matsushita T, et al. FGFR3 promotes synchondrosis closure and fusion of ossification centers through the MAPK pathway. Human molecular genetics. 2009; 18:227–240. doi:10.1093/hmg/ddn339. [PubMed: 18923003]
64. Matsushita T, et al. Extracellular signal-regulated kinase 1 (ERK1) and ERK2 play essential roles in osteoblast differentiation and in supporting osteoclastogenesis. Molecular and cellular biology. 2009; 29:5843–5857. doi:10.1128/MCB.01549-08. [PubMed: 19737917]
65. Guntur AR, Rosen CJ. IGF-1 regulation of key signaling pathways in bone. Bonekey Rep. 2013; 2:437. doi:10.1038/bonekey.2013.171. [PubMed: 24422135]
66. Gerber HP, et al. VEGF couples hypertrophic cartilage remodeling, ossification and angiogenesis during endochondral bone formation. Nature medicine. 1999; 5:623–628. doi:10.1038/9467.
67. Zelzer E, et al. VEGFA is necessary for chondrocyte survival during bone development. Development. 2004; 131:2161–2171. doi:10.1242/dev.01053. [PubMed: 15073147]
68. Duan X, et al. Vegfa regulates perichondrial vascularity and osteoblast differentiation in bone development. Development. 2015; 142:1984–1991. doi:10.1242/dev.117952. [PubMed: 25977369]
69. Borjesson AE, Lagerquist MK, Windahl SH, Ohlsson C. The role of estrogen receptor alpha in the regulation of bone and growth plate cartilage. Cell Mol Life Sci. 2013; 70:4023–4037. doi: 10.1007/s00018-013-1317-1. [PubMed: 23516016]
70. Zhang X, et al. Epidermal growth factor receptor (EGFR) signaling regulates epiphyseal cartilage development through beta-catenin-dependent and -independent pathways. The Journal of

biological chemistry. 2013; 288:32229–32240. doi:10.1074/jbc.M113.463554. [PubMed: 24047892]

71. Morita K, et al. Reactive oxygen species induce chondrocyte hypertrophy in endochondral ossification. The Journal of experimental medicine. 2007; 204:1613–1623. doi:10.1084/jem.20062525. [PubMed: 17576777]
72. Koretsi V, Kirschneck C, Proff P, Romer P. Expression of glutathione peroxidase 1 in the spheno-occipital synchondrosis and its role in ROS-induced apoptosis. European journal of orthodontics. 2015; 37:308–313. doi:10.1093/ejo/cju045. [PubMed: 25312980]
73. Kim KS, Choi HW, Yoon HE, Kim IY. Reactive oxygen species generated by NADPH oxidase 2 and 4 are required for chondrogenic differentiation. The Journal of biological chemistry. 2010; 285:40294–40302. doi:10.1074/jbc.M110.126821. [PubMed: 20952384]
74. Ahmad R, Sylvester J, Ahmad M, Zafarullah M. Involvement of H-Ras and reactive oxygen species in proinflammatory cytokine-induced matrix metalloproteinase-13 expression in human articular chondrocytes. Archives of biochemistry and biophysics. 2011; 507:350–355. doi:10.1016/j.abb.2010.12.032. [PubMed: 21211511]
75. Pauws E, et al. Tbx22null mice have a submucous cleft palate due to reduced palatal bone formation and also display ankyloglossia and choanal atresia phenotypes. Human molecular genetics. 2009; 18:4171–4179. doi:10.1093/hmg/ddp368. [PubMed: 19648291]
76. Parada C, et al. Disruption of the ERK/MAPK pathway in neural crest cells as a potential cause of Pierre Robin sequence. Development. 2015 doi:10.1242/dev.125328.
77. Sandham A, Cheng L. Cranial base and cleft lip and palate. The Angle orthodontist. 1988; 58:163–168. doi:10.1043/0003-3219(1988)058<0163:CBACLA>2.0.CO;2. [PubMed: 3164594]
78. Horswell BB, Gallup BV. Cranial base morphology in cleft lip and palate: a cephalometric study from 7 to 18 years of age. Journal of oral and maxillofacial surgery : official journal of the American Association of Oral and Maxillofacial Surgeons. 1992; 50:681–685. discussion 686.
79. Harris EF. Size and form of the cranial base in isolated cleft lip and palate. The Cleft palate-craniofacial journal : official publication of the American Cleft Palate-Craniofacial Association. 1993; 30:170–174. doi:10.1597/1545-1569(1993)030<0170:SAFOTC>2.3.CO;2. [PubMed: 8452839]
80. Ross RB. My friend the cranial base: why is it so normal? The Cleft palate-craniofacial journal : official publication of the American Cleft Palate-Craniofacial Association. 1993; 30:511–512. doi:10.1597/1545-1569(1993)030<0511:MFTCBW>2.3.CO;2. [PubMed: 8218317]
81. Beaty TH, et al. Analysis of candidate genes on chromosome 2 in oral cleft case-parent trios from three populations. Human genetics. 2006; 120:501–518. doi:10.1007/s00439-006-0235-9. [PubMed: 16953426]
82. Devoto M, et al. First-stage autosomal genome screen in extended pedigrees suggests genes predisposing to low bone mineral density on chromosomes 1p, 2p and 4q. European journal of human genetics : EJHG. 1998; 6:151–157. doi:10.1038/sj.ejhg.5200169. [PubMed: 9781060]
83. Niu T, et al. A genome-wide scan for loci linked to forearm bone mineral density. Human genetics. 1999; 104:226–233. [PubMed: 10323246]
84. Wynne F, et al. Suggestive linkage of 2p22-25 and 11q12-13 with low bone mineral density at the lumbar spine in the Irish population. Calcified tissue international. 2003; 72:651–658. doi:10.1007/s00223-002-2086-2. [PubMed: 14562992]
85. Pope FM, Nicholls AC, McPheat J, Talmud P, Owen R. Collagen genes and proteins in osteogenesis imperfecta. Journal of medical genetics. 1985; 22:466–478. [PubMed: 3001313]
86. Prockop DJ, et al. Mutations in osteogenesis imperfecta leading to the synthesis of abnormal type I procollagens. Annals of the New York Academy of Sciences. 1985; 460:289–297. [PubMed: 3868953]
87. Lapunzina P, et al. Identification of a frameshift mutation in Osterix in a patient with recessive osteogenesis imperfecta. American journal of human genetics. 2010; 87:110–114. doi:10.1016/j.ajhg.2010.05.016. [PubMed: 20579626]
88. Cheung MS, et al. Cranial base abnormalities in osteogenesis imperfecta: phenotypic and genotypic determinants. Journal of bone and mineral research : the official journal of the American Society for Bone and Mineral Research. 2011; 26:405–413. doi:10.1002/jbmr.220.

89. McLeod MJ. Differential staining of cartilage and bone in whole mouse fetuses by alcian blue and alizarin red S. Teratology. 1980; 22:299–301. doi:10.1002/tera.1420220306. [PubMed: 6165088]

90. Jegalian BG, De Robertis EM. Homeotic transformations in the mouse induced by overexpression of a human Hox3.3 transgene. Cell. 1992; 71:901–910. [PubMed: 1360874]

91. Garcia-Garcia MJ, et al. Analysis of mouse embryonic patterning and morphogenesis by forward genetics. Proceedings of the National Academy of Sciences of the United States of America. 2005; 102:5913–5919. doi:10.1073/pnas.0501071102. [PubMed: 15755804]

92. Kasarskis A, Manova K, Anderson KV. A phenotype-based screen for embryonic lethal mutations in the mouse. Proceedings of the National Academy of Sciences of the United States of America. 1998; 95:7485–7490. [PubMed: 9636176]

93. Lewandoski M, Meyers EN, Martin GR. Analysis of Fgf8 gene function in vertebrate development. Cold Spring Harbor symposia on quantitative biology. 1997; 62:159–168. [PubMed: 9598348]

94. Rodriguez CI, et al. High-efficiency deleter mice show that FLPe is an alternative to Cre-loxP. Nature genetics. 2000; 25:139–140. doi:10.1038/75973. [PubMed: 10835623]

95. Simmons O, Bolanis EM, Wang J, Conway SJ. In situ hybridization (both radioactive and nonradioactive) and spatiotemporal gene expression analysis. Methods in molecular biology. 2014; 1194:225–244. doi:10.1007/978-1-4939-1215-5_12. [PubMed: 25064106]

96. Pabst O, Rummelies J, Winter B, Arnold HH. Targeted disruption of the homeobox gene Nkx2.9 reveals a role in development of the spinal accessory nerve. Development. 2003; 130:1193–1202. [PubMed: 12571110]

97. Dodd J, Morton SB, Karagogeos D, Yamamoto M, Jessell TM. Spatial regulation of axonal glycoprotein expression on subsets of embryonic spinal neurons. Neuron. 1988; 1:105–116. [PubMed: 3272160]

98. Cardiff RD, Miller CH, Munn RJ. Manual hematoxylin and eosin staining of mouse tissue sections. Cold Spring Harbor protocols. 2014; 2014:655–658. doi:10.1101/pdb.prot073411. [PubMed: 24890205]

99. Chai Y, et al. Fate of the mammalian cranial neural crest during tooth and mandibular morphogenesis. Development. 2000; 127:1671–1679. [PubMed: 10725243]

100. Schneider CA, Rasband WS, Eliceiri KW. NIH Image to ImageJ: 25 years of image analysis. Nature methods. 2012; 9:671–675. [PubMed: 22930834]

Highlights

- Forward genetic screen isolates MEMO1 as a key factor in craniofacial development
- MEMO1 drives cranial base and palatal development
- High levels of Memo1 expression localized to bones in the developing head
- MEMO1 shown to promote cartilage to bone turnover in the cranial base
- MEMO1 functions autonomously during ossification of anterior cranial base

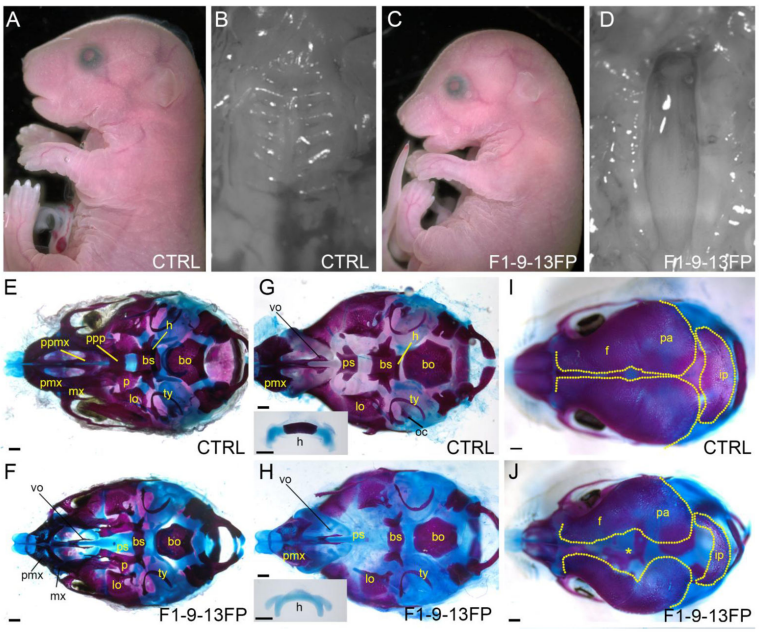

Figure 1. The F1-9-13FP craniofacial phenotype

(A-D) E18.5 control (A, B) or F1-9-13FP (C, D) mouse embryo, either shown in lateral view (A, C) or a ventral view of the secondary palate (B, D). **(E-J)** E18.5 craniofacial skeletal preparations of either a control (E, G, I) or F1-9-13FP mutant (F, H, J), shown in ventral views with the mandible removed (E, F), mandible plus palatal bones removed (G, H), or dorsal view of the developing calvaria (I, J). Inset in G and H is the hyoid skeletal element shown in isolation. Abbreviations: bs, basisphenoid; bo, basioccipital; f, frontal; h, hyoid; ip, interparietal; lo, lamina obturans; mx, maxillary; oc, otic capsule; p, palatine; pa, parietal; pmx, premaxillary; ppmx, palatal process of maxilla; ppp, palatal process of palatine; ps, presphenoid; ty, tympanic; vo,vomer. The "*" in panel J indicates the enlarged space between the frontal bones of the mutant. Scale bar: 500uM.

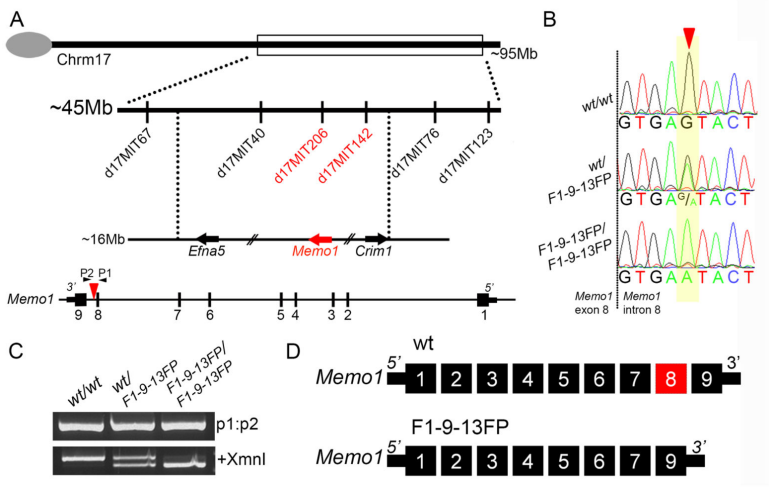

Figure 2. Mapping and exome sequencing identifies a point mutation in *Mediator of ErbB2 driven cell motility 1* associated with the F1-9-13FP phenotype

A) Top: Schematic of mouse chromosome 17 showing markers used to map the position of the ENU induced mutation in F1-9-13FP embryos. Bottom: Schematic of the *Memo1* locus showing relative location of point mutation (red arrowhead in intron 8). Note direction of transcription is shown from right to left to match chromosomal arrangement. **B)** Representative chromatograms of sequencing results from genomic DNA of wild-type as well as F1-9-13FP heterozygous and homozygous embryos, with position of the single nucleotide transition in intron 8 of *Memo1* shown by red arrowhead. **C)** Gel electrophoresis of PCR products generated using primers (P1 and P2 in Fig 2A) flanking the ENU induced mutation and genomic DNA from wild-type as well as F1-9-13FP heterozygous and homozygous embryos. Prior to size separation a portion of the PCR product was digested with XmnI restriction enzyme (lower gel). **D)** Schematic of the nine exon wild-type *Memo1* mRNA transcript as well as the major mRNA splice product produced in F1-9-13FP mutants, namely an in-frame deletion of the exon 8 (for clarity, the orientation of the transcript has been reversed from that shown in A).

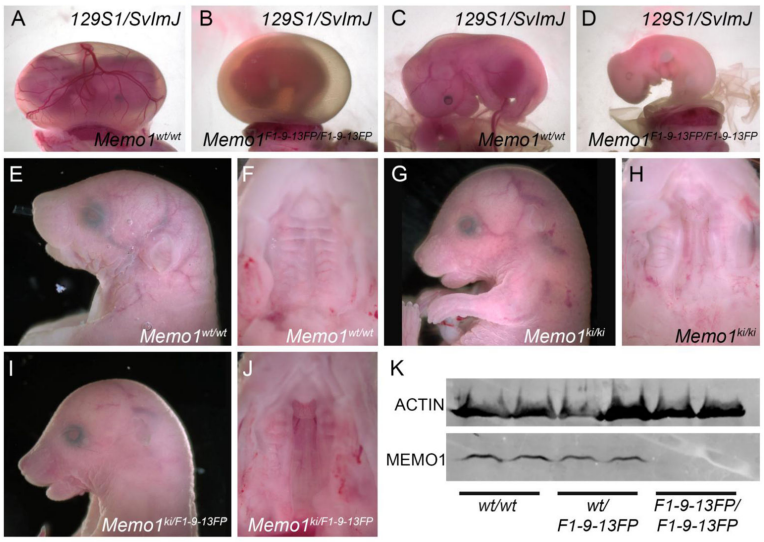

Figure 3. F1-9-13FP generates a null mutation in *Memo1* that is subject to genetic background effects

(A-D) An E14.5 control (A, C) or *Memo1*^{m1Will} mutant (B, D) on the 129S1/SvlmJ genetic background showing the intact yolk-sac (A, B) or a lateral view of the embryo proper (C, D). **(E-J)** E18.5 mouse embryos, of the genotypes indicated, from a largely C57BL/6J background showing lateral views of the head (E, G, I) or ventral views of the secondary palate after the mandible has been removed (F, H, J). (K) Western blot analysis of protein isolated from E13.5 heads of wild-type, heterozygous, or homozygous F1-9-13FP mutants, and probed with an anti-MEMO1 antibody (anti-ACTIN used as a loading control, one embryo per lane).

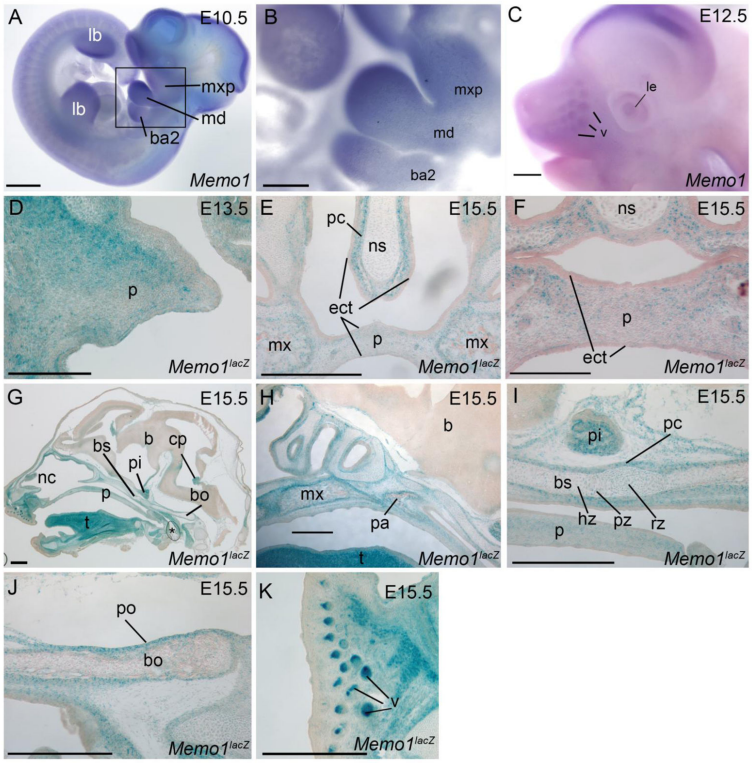

Figure 4. Embryonic expression of *Memo1* during craniofacial development

(A-C) Lateral views of embryos processed by whole-mount *in situ* hybridization using an anti-sense *Memo1* riboprobe at E10.5 (A, B) and E12.5 (C). Note, (B) is boxed region in (A) shown at higher magnification. **(D-K)** b-galactosidase staining (blue) of frozen *Memo1*$^{neo/+}$ sections at the time points indicated in either a frontal (D-F) or sagittal (G-K) plane, counterstained with nuclear fast red. A single palatal shelf is shown at E13.5, prior to fusion (D), or both shelves at E15.5 subsequent to secondary palatal fusion (E, F). Note, E is slightly more posterior than F. Additional images from E15.5 show a midsagittal plane of the entire embryonic head (G) or detailed images of the secondary palate and anterior cranial base (H), mid-cranial base (I), posterior cranial base (J), and snout (K). Orientation for (G-K) is rostral left, caudal right. Abbreviations: b, brain; ba2, branchial arch 2; bs, basisphenoid; bo, basioccipital; cp, choroid plexus; ect, ectoderm; hz, hypertrophic zone; lb, limb bud; le, lens; md, mandibular prominence; mx, maxilla; mxp, maxillary prominence; nc, nasal cavity; ns, nasal septum; p, palate; pa, palatine bone; pc, perichondrium; pi, pituitary gland; po, periosteum; pz, proliferative zone; rz, resting zone; t, tongue; v, vibrissae. Note, asterisk in G. highlights air bubble from processing. Scale bars: A, C, E, G-K: 500uM; B: 125uM; D, F: 200uM

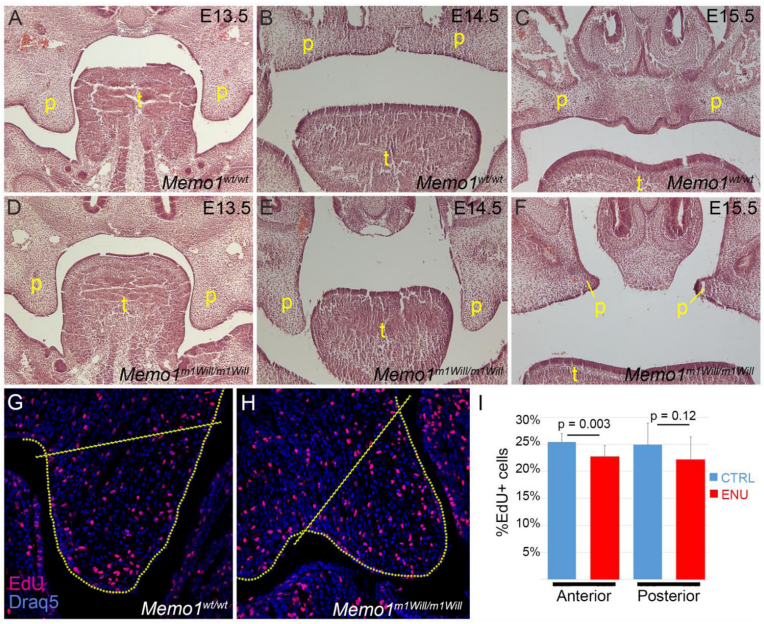

Figure 5. *Memo1*^{m1Will} mutant embryos undergo a failure of palatal shelf elevation and show a modest reduction in mesenchymal cell proliferation in the palatal shelves

(A-F) H&E stained frontal sections midway through the developing palate of control (A-C) or *Memo1*^{m1Will} mutant (D-F) embryos at the time point indicated. **(G, H)** Representative images of frontal sections through the anterior palatal shelf at E13.5 in a control (G) or *Memo1*^{m1Will} mutant (H) embryo that have been processed for EdU immunoreactivity to mark proliferative cells. Area internal to dashed lines indicates region quantified in I. **(I)** Total number of proliferating cells relative to the total cell number in the palatal shelf mesenchyme was quantified between control and *Memo1*^{m1Will} mutant embryos in both anterior and posterior positions of the developing palate. (N = 3 embryos per group, 10-12 individual palatal shelves [3-4 per embryo] per location). Abbreviations: p, palate; t, tongue.

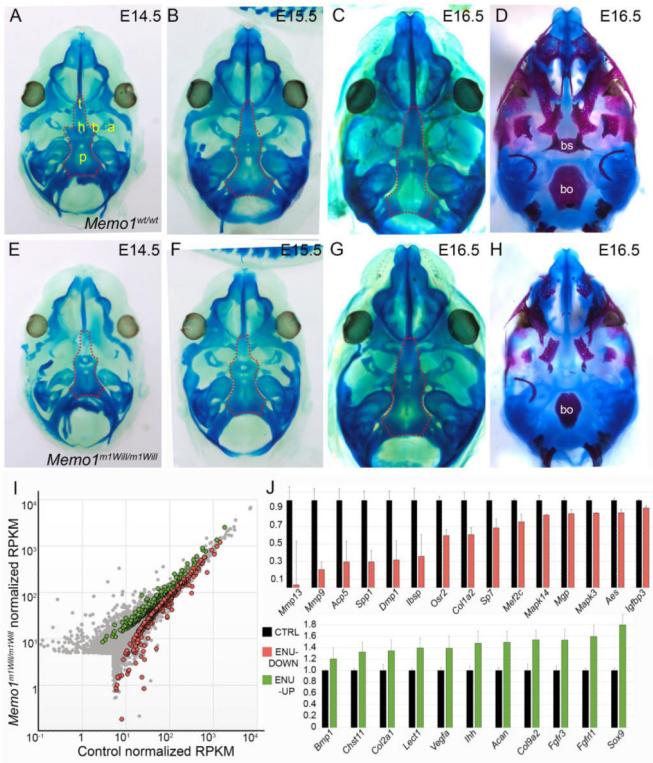

Figure 6. *Memo1*^{m1Will} mutants show normal chondrocranium development but reduction in regulators of endochondral ossification in the cranial base

(A-H) Ventral views of the developing cranial base with mandible removed, in control (A-D) or *Memo1*^{m1Will} mutants (E-H). Samples are stained with either alcian blue alone for cartilage (A-C, E-G), with the dotted outline highlighting the cranial base, or alcian blue plus alizarin red, marking cartilage and bone (D, H). **(I)** Scatter plot depicting average RPKM (reads per kilobase per million mapped reads) values of RNAseq conducted on RNA isolated from E15.5 cranial bases (similar to outlined area in B and F) of control (X-axis) or *Memo1*^{m1Will} mutants (Y-axis) (3/group). Colored points represent transcripts that are statistically significant between groups (Green: up-regulated in *Memo1*^{m1Will}, ~220 genes; and red: down-regulated ~300 genes). **(J)** Upper panel: histogram plotting normalized RPKM values of genes associated with endochondral ossification and significantly down-regulated in *Memo1*^{m1Will} mutant cranial base samples as compared to controls. Lower panel: same as upper panel, but plotting significantly up-regulated genes from *Memo1*^{m1Will} cranial base samples as compared to controls and associated with cartilage development. Error bars represent standard error calculated from 3 replicates. Abbreviations: a, ala temporalis cartilage; b, basitrabecular process; bo, basioccipital; bs, basisphenoid; h, hypophyseal cartilage; p, parachordal cartilage; t, trabecular cartilage (trabecular plate).

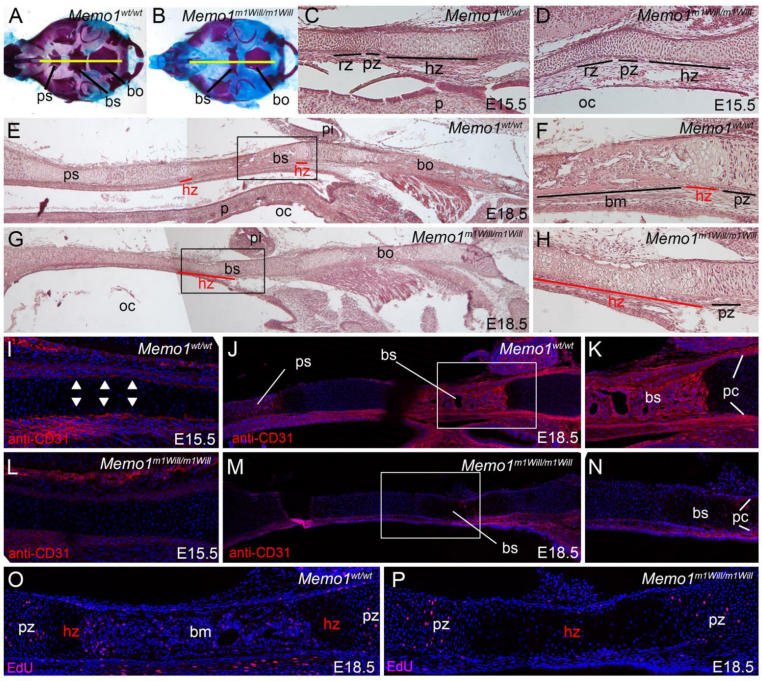

Figure 7. Reduced ossification in the cranial base of *Memo1*^{m1Will} mutants is associated with an elongated hypertrophic chondrocyte zone and reduced vascular invasion

Analysis of the cranial base skeleton at E15.5 (C, D, I, L) and E18.5 (A, B, E-H, J-K, M-P) for the genotypes indicated shown as either whole mount (A, B) or midsagittal sections (C-P). For all images, rostral is to the left and caudal to the right. (**A, B**) Craniofacial skeletons used to diagram approximate position of sections (yellow line) through the cranial base. Note, skeletons shown are E18.5, although similar sections were used at E15.5. (**C, D**) H&E stained sections, focusing on the developing basisphenoid bone. (**E-H**) H&E stained sections, focusing on the entire cranial base (E, G) or the basisphenoid bone alone (F, H). Note, F and H are higher magnification images of the boxed regions in E and G. (**I-N**) anti-CD31 stained frozen sections, focusing on the developing basisphenoid bone. Note, K and N are higher magnification images of the boxed regions in J and M. Arrowheads in (I) highlight perichondrial staining. (**O, P**) EdU staining, marking proliferating cells, in the basisphenoid bone and flanking cartilage. Note, for sections in I-P, nuclei were counterstained with DRAQ5. Abbreviations: bm, bone matrix; bo, basioccipital; bs, basisphenoid; hz, hypertrophic zone; oc, oral cavity; p, palate; pi, pituitary; pc, perichondrium; ps, presphenoid; pz, proliferative zone; rz, resting zone.

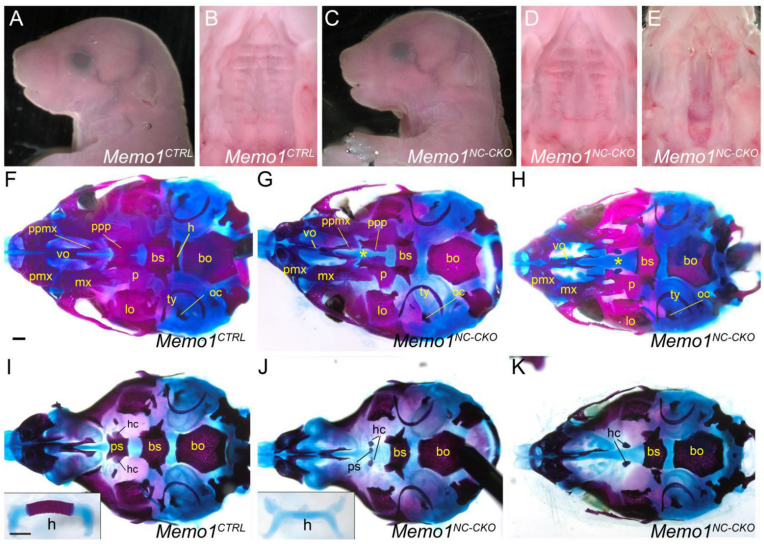

Figure 8. MEMO1 has a cell-autonomous function within neural crest cells for cranial base ossification but not for palatal shelf fusion

(A-E) E18.5 mouse embryo of the genotype indicated, either shown in lateral view (A and C) or a ventral view of the secondary palate (B, D, and E). **(F-K)** E18.5 craniofacial skeletal preparations of either control (F, I) or *Memo1*$^{NC\text{-}CKO}$ embryos (G, H, J, K), shown in ventral views with either the mandible (F-H) or mandible plus palatal bones (I-K) removed. Insets in I and J show the hyoid element in isolation. "*" denotes region of hypoplastic development of palatal processes (maxillary and palatine bones). Abbreviations: bs, basisphenoid; bo, basioccipital; h, hyoid; hc, hypochiasmatic cartilage; lo, lamina obturans; mx, maxilla; oc, otic capsule; p, palatine; pmx, premaxilla; ppmx, palatal process of maxilla; ppp, palatal process of palatine; ps, presphenoid; ty, tympanic ring; vo, vomer. Scale bars: 500uM.

Table 1

Summary of F1-9-13FP genotype frequencies at E18.5 and P21

	E18.5		P21	
Genotype	**Observed**[#]	**Expected**	**Observed**[&]	**Expected**
wt/wt	37	31.5	22	18
wt/F1-9-13FP	70	63	50	36
F1-9-13FP/F1-9-13FP	19[*]	31.5	0	18
Total	126	$\chi^2 = 0.035$	72	$\chi^2 = 5.201E-06$

χ^2 analysis at E18.5 indicates that homozygous mutant numbers are lower than expected, suggesting some embryos are lost earlier in embryogenesis.

[#]Counts are based on > 95% C57BL/6J background

[&]Counts are based on > 85% C57BL/6J background

[*]gross external examination indicated that 19/19 displayed reported craniofacial phenotypes, while 7/19 had some evidence of vasculature defects including edema and purpura (data not shown)